NEONATAL MONITORING WITH FMCW MILLIMETER WAVE RADAR

MASTER THESIS REPORT

NEONATAL MONITORING WITH FMCW MILLIMETER WAVE RADAR

MASTER THESIS REPORT

Dissertation

to obtain the degree of Master of Science
in Electrical Engineering
at Delft University of Technology
to be defended publicly on Wednesday August 30, 2023 at 15:00 PM

by

Jialin LYU

born in Jinan, China.

This thesis has been approved by

Supervisor: Dr. Francesco Fioranelli

Thesis committee:

Dr. Francesco Fioranelli,	EWI-ME-MS3, TU Delft
Dr. Marco Spirito,	EWI-ME-ELCA, TU Delft

ACKNOWLEDGEMENTS

Times will fly, things will change, but I will always cherish the memories of the two years I spent studying and living at TU Delft. And I would like to express my deepest gratitude to the following individuals and groups for their invaluable support and contributions throughout this journey.

First and foremost, I am immensely grateful to my thesis supervisor, Dr. Francesco Fioranelli, for the professional guidance and enthusiastic encouragement he has provided during this wonderful journey. Each week when I met with him, he provided me with valuable advice that enhanced my work efficiency and deepened my comprehension of the thesis project. He consistently displayed a high level of responsiveness, even during his vacations, promptly addressing my inquiries, revising my writing drafts, and guiding me to write in an academic manner. Being guided by him is indeed a pleasure, and his mentorship will always be invaluable in my future career.

I would also like to express my gratitude to all the professors, PhDs, and MSc students at the Microwave Sensing, Signals, and Systems Group. Together, they have cultivated a harmonious and dynamic atmosphere within MS3. Their active participation, thoughtful inquiries, and invaluable insights during our Friday meetings have significantly contributed to the advancement of my research. My sincere thanks extend to the six volunteers who generously assisted me with my experiment, without whom I would not have been able to complete my project. Moreover, I would like to thank Caitlin Ramsey from Terahertz Sensing Group, for being willing to share the radar recording of real neonates with me, making it possible to validate the proposed pipeline in this thesis project.

Also, I would like to thank Dodo Ye for the care and attention that I received during my graduation. Thanks to all my friends, especially Huanqiang Duan and Qing Zhang for their long-lasting companionship and sincere friendship during the years spent in the Netherlands. And heartfelt thanks to my family, whose unwavering support and unconditional love have served as my anchor throughout this challenging journey! Without you, I couldn't have achieved this. Thank you from the bottom of my heart!

Thank you all for being part of this memorable and fruitful journey! Last but not least, citing a famous line from the movie *The Truman Show*, "**Good morning, and in case I don't see you, Good afternoon, Good evening, And good night**" to wish you the most profound blessings.

Jialin Lyu
Delft, August 2023

ABSTRACT

According to the World Health Organization, approximately 15 million neonates are born prematurely each year, which is more than 1 in 10 newborns. Premature birth disrupts the normal development of the neonate in the womb, which can result in various complications and health issues, necessitating continuous monitoring of vital signs to assess their health status.

Currently, the predominant monitoring approach involves the use of contact-wired sensors, which offer precise readings but are accompanied by specific drawbacks. One notable limitation is the utilization of strong adhesives to attach the sensor to the neonate's skin, causing pain and stress during removal. Additionally, the wired sensor hinders skin-to-skin contact care, which is proved to be crucial for the neonate's growth and development.

To address these drawbacks, a non-contact wireless approach using FMCW radar is proposed in this thesis project. The main aim is to develop a processing pipeline to monitor the vital signs of neonates with the radar. The core concept involves estimating the vital signs from the phase information corresponding to the chest movement of the monitoring target. This will be achieved through the implementation of an algorithm based on the short-time Fourier transform. Furthermore, this study also explores an approach to detect body movement, select near-steady state data segment and determine the range bin that is most relevant for the vital signs estimation.

The proposed pipeline aims to provide a more comfortable and efficient monitoring system for neonates, potentially overcoming the limitations of conventional contact-wired sensors and promoting better care for their overall well-being and development.

CONTENTS

List of Figures

List of Tables

ABBREVIATIONS

BMI	body mass index
bpm	breaths per minute
bpm	beats per minute
CRLB	Cramer-Rao Lower Bound
CS	compressed sensing
CV	coefficient of variation
CW	continuous wave
CWT	continuous wavelet transform
ECG	electrocardiography
EEMD	ensemble empirical mode decomposition
FFT	fast Fourier transform
FMCW	frequency-modulated continuous-wave
GMM	Gaussian Mixture Model
GUI	graphical user interface
HR	heartbeat rate
IMFs	intrinsic mode functions
IP	impedance pneumography
IR-UWB	impulse radio ultra-wide band
KF	Kalman filter

LMS	least mean square
LoA	Limits of Agreement
LTS	linear trend subtraction
MFCCs	mel-frequency cepstral coefficients
MHOC-FFT	multifold high order cumulant fast Fourier transform
MIMO	multiple-input multiple-output
MPC	magnitude-phase coherency
MRC	maximum ratio combing
MS	mean subtraction
MUSIC	multiple signal classification
NICU	Neonatal Intensive Care Unit
NMF	non-negative matrix factorization
PC	pulsed coherent
PCC	Pearson correlation coefficient
PD	parameterized demodulation
PSD	power spectrum density
RBM	random body movements
RLS	recursive least squares
RMS	root mean square
RPC	reproducibility coefficient
RPS	range profile subtraction
RR	respiration rate
SNR	signal-to-noise ratio

STFT	short-time Fourier transform
SVD	singular value decomposition
UWB	ultra-wide band
VMD	variational mode decomposition
WHO	World Health Organization
WT	wavelet transform

1

INTRODUCTION

This chapter provides the comprehensive background behind the vital signs monitoring of the neonate in Section 1.1. Subsequently, the problem statement of this thesis is defined in Section 1.2 based on the existing gaps found in the relevant researches, and Section 1.3 summarizes the main contributions of the proposed radar signal processing pipeline, which is used to estimate vital signs of the neonate in this thesis. Last but not least, the structure of this thesis is presented in Section 1.4

1.1. PROJECT BACKGROUND

According to the World Health Organization (WHO), an estimated 15 million neonates are born preterm every year, that is more than 1 in 10 neonates [1]. Those preterm neonates are born before 37 completed weeks of gestation, which means the loss of development time in the womb disrupts their growth. Consequently, their organ systems and associated functions, as well as their immune system are immature, which is the primary reason why these neonates are facing a higher risk of infections, chronic diseases, and respiratory problems, so called the preterm birth complication [2], [3].

A significant consequence is that the immaturity of breathing regulation and lungs often leads to apnea-bradycardia and respiratory distress syndromes. This is commonly followed by bronchopulmonary dysplasia in 27% of the neonates born at less than 30 weeks of gestation [3], [4]. Additionally, there are numerous other preterm birth complications, which are the leading cause of death among children under 5 years of age, responsible for approximately 1 million deaths each year. Even for those who survive, they may still face a lifetime of disability, including learning disabilities and visual and hearing problems [5]. Such lifetime disabilities not only impact the affected individuals but also place a heavy burden on their families. As a means of preventing the preterm birth complications and allowing the preterm neonates to develop in a healthy environment outside the womb, preterm neonates are often required to spend several weeks in the Neonatal Intensive Care Unit (NICU).

During this period, it is mandatory to have continuous monitoring of the neonates' vital signs, and some of the most important parameters are the respiration rate (RR) and

the heartbeat rate (HR)[3]. RR of neonates is commonly monitored using impedance pneumography (IP), which measures the changes in electrical impedance resulting from aeration of the lung and movement of the chest wall through electrodes attached to the chest skin [6]. On the other hand, HR of neonates is typically monitored by electrocardiography (ECG), which also relies on electrodes placed on the skin to measure the electrical changes that are a consequence of cardiac muscle depolarization followed by repolarization during each cardiac cycle [7]. An example of those conventional contact-based approaches, which directly attach the electrode as the sensor to the fragile skin of the neonates and are connected to the monitoring systems through wires, is shown in Figure 1.1. Even if the system truly returns accurate numbers, it still can cause other problems, such as skin irritation to the neonates and might eventually lead to pressure necrosis. Besides, it is also important for nurses and parents to have skin-to-skin contact care for the neonates, which has been shown to be extremely beneficial for their growth. However, those wired contact sensors make it difficult for the nurse to hold the neonates while doing the skin to skin contact care. Moreover, the wires also restrict the natural movement of the neonates, and it has been proven to add stress which may hinder their development process [8].

Figure 1.1: Wired contact sensor attached to the neonate [9]

1.2. PROBLEM STATEMENT

As mentioned above, despite the wired contact sensors can measure the vital signs accurately, there are still some glaring drawbacks, which are supposed to be fixed to promote the development of preterm neonates in the future. Therefore, contact-less vital signs monitoring is an area of interest to fill the gap, which attracts more and more attention and effort. Currently, a variety of contact-less approaches are being developed to be capable of monitoring vital signs for the neonates.

For example, RR and HR monitoring in preterm neonates is reported in a study by Villarroel et al [10] using a digital video camera by monitoring the color and volume changes in superficial blood vessels during the cardiac cycle. But one of the most important elements for the monitoring is the ambient light, which means such a method cannot be used all the time. Another study conducted on preterm neonates for monitoring RR with an infrared thermal camera, based on analysis of the anterior nares temperature

profile associated with the inspiration and expiration phases successively is reported by Abbas et al [11]. Major pitfalls of the infrared thermography-based method, include the need for higher resolution images, the effect of surrounding temperature variations and costly equipment [12].

Comparing with the digital video camera, the radar-based sensors have advantages, such as being independent of changes in the ambient light and the subject skin complexion. As for the infrared thermography-based method, the radar-based sensors are not affected by ambient temperature, while being relatively price friendly for future implementation in low-budget cases [12]. Therefore, the main problem to be addressed in this thesis work is formulated as follows:

"**Develop, validate and evaluate a proof of concept processing pipeline based on radar technology to identify the target data segments, locate the target position and estimate the respiration rate (RR) and the heartbeat rate (HR) of the neonates. To begin with, the proposed processing pipeline will be developed, verified and evaluated for adult vital signs monitoring under ideal scenarios. After that, the proposed processing pipeline will be promoted to work and test at the real conditions for neonate vital signs monitoring.**"

To be more specific, the proposed processing pipeline is used to monitor RR and HR when the neonates are in a near-steady state. Therefore, the initial step involves identifying data segments without large body movement by body movement detection approaches. And these segments will serve as the target data for the pipeline to process. The next step is to locate the target position, which means automatically selecting the most relevant range bin in the range-time map to gather information for further estimation.

When transitioning from monitoring adult to neonate, capturing the respiration and heartbeat becomes more challenging due to the difference in body sizes. Therefore, the smaller size of neonates presents technical difficulties in accurately capturing RR and HR using radar technology. Besides, unlike cooperative adult, the neonate cannot stay in a steady state while collecting the data, which makes it more important to identify the steady state data segments for further processing.

Last but not least, another important point to mention is that there is an experimental dataset of neonates' radar data, which was collected by C. Ramsey at the NICU of Erasmus Medical Center as part of a joint research project with TU Delft within the Convergence Framework [13]. The dataset was collected when the neonates were lying in an open bed crib covered in clothing and blanket, similar to incubator care, as described in [8]. For this thesis project, the dataset from C. Ramsey will be used to validate and evaluate the proposed processing pipeline.

1.3. CONTRIBUTION OF THE THESIS

The main contributions of the work in this thesis are:

1) A pre-process procedure that can detect the body movement of the target, segment the data based on the body movement, and identify appropriate data segments is formulated. An automatic approach used to locate the target position by selecting the most relevant range bin in the range-time map is also generated. A short-time

Fourier transform (STFT) based algorithm is implemented to estimate RR and HR of those appropriate data segments.

2) The proposed processing pipeline is validated and evaluated through a combination of mathematical model simulations and experiments. In the experiment part, a 60 GHz frequency-modulated continuous-wave (FMCW) multiple-input multiple-output (MIMO) radar is used. The radar waveform design process is discussed and a basic radar waveform is designed for the radar, using to collect the adult data. The experimental dataset is collected from 6 adult volunteers and 6 neonates, allowing for a comprehensive assessment of the pipeline's performance and effectiveness.

3) After processing the data, there are acceptable results in terms of simulations, adult experiments and neonate experiments, which have mean absolute errors less than 0.06 Hz and 0.15 Hz for RR and HR respectively. An exploration about the impact of different channel data of the MIMO radar on the monitoring performance is discussed.

1.4. STRUCTURE OF THE THESIS

The structure of the thesis is as follows. Chapter 2 describes the relevant literature related to vital signs monitoring through radar technology. Besides, there are also different approaches used to identify the target data segments and locate the target position, mainly including two procedures, body movement detection and range bin selection. By presenting examples of real data processing, Chapter 3 introduces the proposed processing pipeline used to monitor the vital signs of the target. In Chapter 4, the simulation of the vital signs based on the mathematical models is used to validate the pipeline. Moreover, a Monte Carlo test is also implemented to evaluate the pipeline. The laboratory measurement setup for data acquisition for both adult and neonate is fully described in Chapter 5. Furthermore, the data process and result analysis for both adult and neonate datasets are illustrated in Chapter 6. Last but not least, the corresponding conclusion together with the outlines for potential future work are summarized in Chapter 7.

2

LITERATURE REVIEW

In this chapter, the relevant works regarding respiration and heartbeat monitoring through radar technology are presented. In Section 2.1, mathematical signal models for cardiopulmonary activity are introduced for further simulation work in Chapter 4. Afterwards, the following sections are describing the main steps, which are commonly used in vital signs monitoring. First, the important procedure used to remove stationary clutter of the range-time map is studied in Section 2.2. While approaches used to detect the body movement and select the range bin for further phase information extraction are studied in Section 2.3 and Section 2.4 respectively. Section 2.5 describes the recent advances in respiration and heartbeat estimation techniques with radar implementation. At the end of this chapter, a summary of the literature review on vital signs monitoring is shown in Section 2.6.

2.1. MATHEMATICAL SIGNAL MODELS FOR CARDIOPULMONARY ACTIVITY

Physiologically, the cardiopulmonary activity consists of two components, respiration and heartbeat. As a result, there will be volumetric changes in the heart muscle and main respiratory muscles, which can be used to extract the cardiopulmonary signal [14]. Therefore, in this section, the mathematical signal model of cardiopulmonary activity is divided into two separate models, one for respiration and another for heartbeat.

2.1.1. RESPIRATION MODEL

The most fundamental function of the human respiratory system is to complete the gas exchange, which is to release carbon dioxide from the capillaries into the alveoli while diffusing oxygen into the capillaries at the blood-gas barrier [15]. In order to finish the gas exchange, a complete breathing cycle, as shown in Figure 2.1, has two main motions, which are the inhalation and the exhalation. During inhalation, the diaphragm becomes flat and gets lowered by the contraction of its muscle fibers, and the intercostal muscles contract and pull the ribs and sternum upward and outward, thus increasing the volume of the thoracic cavity for the lung to expand. When exhaling, the muscle fibers of

diaphragm relax making it convex, the intercostal muscles relax and bring the ribs and sternum to the original position resulting in decreases of the volume of thoracic cavity for the lung to contract [16].

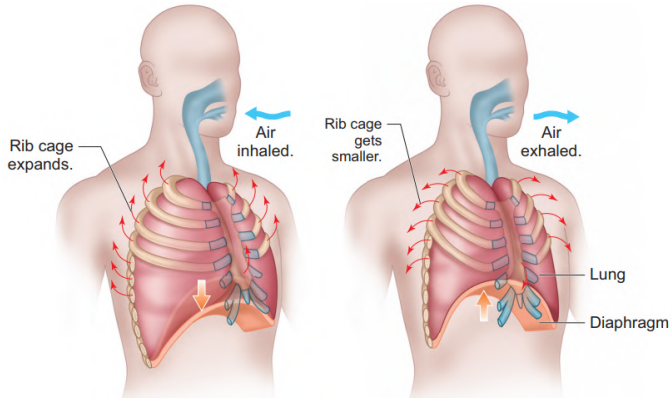

Figure 2.1: Simple physiologic sketch of inhalation and exhalation [16]

Due to the changes of thoracic cavity volume, there will be distinct displacements on the surface of the chest, which can be captured by radar, allowing non-contact measurement of respiration. For healthy adults, standard amplitudes for this motion range between 4 mm and 12 mm [17], with RR varying from 9 to 30 breaths per minute (bpm) [18]. For preterm neonates, these amplitudes can be smaller than 1 mm, while the RR normally stays in 30-80 bpm [19], [20], and reaches up to 110 bpm under specific conditions [21]. Therefore, for the respiration of neonates in this thesis, the amplitudes are assumed to be 0.8-1 mm, while the frequencies are assumed to be 0.5-1.8 Hz.

The most commonly used mathematical model uses the sine or cosine wave with different amplitudes and frequencies to simulate the displacement of the chest over time $R_r(t)$ caused by respiration, which can be expressed as:

$$R_r(t) \approx \frac{\alpha_r}{2} \cdot \left(1 - \cos\left(2\pi f_r \cdot t\right)\right), \tag{2.1}$$

where the α_r denotes the amplitude of the respiration, f_r denotes the frequency of the respiration [22]. Another two alternatives, which are also used to describe the movement of the chest [23], [24], are presented in the following equations:

$$R_r(t) \approx \alpha_r \cdot \sin\left(2\pi f_r \cdot t\right), \tag{2.2}$$

$$R_r(t) \approx \alpha_r \cdot \sin^3\left(2\pi f_r \cdot t\right). \tag{2.3}$$

2.1.2. HEARTBEAT MODEL

The heart plays an essential role in the whole body system of human, and the cardiac cycle is the sequence of events that occurs when the heartbeats [25]. While the heartbeat, it circulates blood through pulmonary and systemic circuits of the body. The cardiac cycle consists of two phases, the diastole phase and the systole phase. As shown in Figure

2.2, in the diastole phase, heart ventricles relax and the heart fills with blood. While in the systole phase, the ventricles contract and pump blood out of the heart to arteries [26]. When the heart contracts to generate the pressure that powers the blood flow, it shifts within the thoracic cavity, striking the chest and producing displacement on the surface of the skin, which is detectable for the radar.

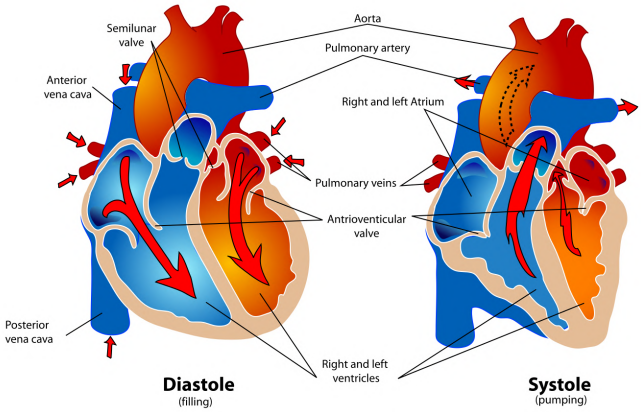

Figure 2.2: Simple physiologic sketch of diastole and systole [26]

For healthy adults, the typical HR lies between 60 to 120 beats per minute (bpm) with an amplitude of approximately from 0.3 mm to 0.8 mm [27]. The HR decreases as neonates get older, for preterm neonates, the HR can be faster than adults varying from 120 to 180 bpm. But the amplitude is much feebler, which can be estimated to be approximately 0.2 mm [28]. Therefore, for the heartbeat of neonates in this thesis, the frequencies are assumed to be 2-3 Hz, while the amplitudes are assumed to be 0.1-0.3 mm.

Same as the respiration, the mathematical model for heartbeat is a cosine wave with different amplitudes and frequencies to simulate the displacement of the chest over time $R_h(t)$ caused by heartbeat, which can be expressed as:

$$R_h(t) \approx \alpha_h \cdot \cos\left(2\pi f_h \cdot t\right). \tag{2.4}$$

where the α_h denotes the amplitude of the heartbeat, f_h denotes the frequency of the heartbeat [22]. Actually, the displacement of the chest caused by heartbeat is much more complicated than cosine waves. To be more accurate, Dennis R. Morgan et al. used a higher-order sinusoidal signal to model the heartbeat[29]. In the thesis, the amplitude scale and the frequency scale of the vital signs for adult and neonate are summarized in the following Table 2.1.

Target	Vital sign	Amplitude [mm]	Frequency [Hz]
Adult	Respiration	4 - 12	0.15 - 0.5
	Heartbeat	0.3 - 0.8	1 - 2
Neonate	Respiration	0.8 - 1	0.5 - 1.8
	Heartbeat	0.1 - 0.3	2 - 3

Table 2.1: Amplitude scale and frequency scale of the vital signs for adult and neonate [19]–[21], [27], [28]

2.2. STATIONARY CLUTTER REMOVAL

In the monitoring scenario, the presence of stationary clutter will cause a static echo in the received signal, which is not linked to the movement of the chest. Such stationary clutter appears as a constant component in the range-time map, which can be manifested as a dc component in the slow time dimension. Consequently, detecting body movement and selecting relevant data segments becomes more challenging due to this constant component. In order to extract the part of the signal that only corresponds to chest motions, it is necessary to remove the static echos of the signal [30]. In other words, a signal pre-processing step to remove stationary clutter is required before generating the input data used for body movement detection.

Various methods can be applied to remove the radar stationary clutter. In [30], [31], the mean subtraction (MS) method, which offers good performance and ease of implementation, is explained. MS calculates the mean of each row over slow time, i.e. the mean of all values obtained in each received chirp at a given time point in the fast time, and then subtracts this value from the corresponding row. As shown in Eq. 2.5, where $RT[r,n]$ represents the range-time map, r denotes the index of range bin, n denotes the index of slow time, for a certain range bin r_i, the range-time map after MS method can be expressed as:

$$RT_{MS}[r_i,n] = RT[r_i,n] - \frac{1}{n}\cdot\sum_{j=1}^{n} RT\left[r_i,j\right]. \tag{2.5}$$

Since the static echo appears in each received signal at the same time positions and more or less with the same amplitude, by subtracting the mean from each row, the static echo is eliminated. On the other hand, the echo due to other moving objects, such as the chest, appears in different time instants of the received signal, so that the mean is different from the samples, and its subtraction does not modify the useful information [32].

Another method, called range profile subtraction (RPS), takes the previous waveform and subtracts it from each newly received waveform, sample by sample [33]. It can be noted that looking at the range dimension of the range-time map, by subtracting the previous sample from the newly arrived sample, it gives a finite difference approximation of the first derivative of the signal [34]. Accordingly, the RPS method acts as a differentiator in the slow time dimension, which can be seen also as a high pass filter, with the impulsive response, the k-th chirp can be expressed as:

$$h[k] = A_k\delta[k] - B_{k-1}\delta[k-1], \tag{2.6}$$

where δ represents the Dirac function, k notes the index of slow time i.e. the slow time instant, and A and B represent the amplitude of the received signal. As noted for the

MS method, a sample will show itself in the same position and with the same amplitude at different slow times only if it belongs to the stationary clutter. If the sample value changes position while moving along the slow time, then it belongs to the chest motion echo of the target. Therefore, by subtracting the previous sample, the static echo can be eliminated [30], [35].

Additionally, there are other methods used to remove the stationary clutter of radar data. For example, the linear trend subtraction (LTS) method is based on estimating the static component and any linear trend long the slow time direction of the range-time map, and on subtracting it from the original data [33], [36]. The singular value decomposition (SVD) splits the data matrix of received waveforms into complementary subspaces each representing different and independent features of the original signals. The purpose of such decomposition is to increase the signal-to-noise ratio (SNR), in order to reduce the effect of the stationary clutter [30]. In [37], a method based on adaptive clutter cancellation applying with a novel dual-frequency impulse radio ultra-wide band (IR-UWB) radar is proposed to eliminate the clutter effect. To summarize the different methods and their respective advantages and disadvantages, Table 2.2 is listed as follows.

Method	**Reference**	**Advantage**	**Disadvantage**
Mean subtraction (MS)	[30], [31]	Good performance, easy to implement	Not applicable for long term data
Range profile subtraction (RPS)	[34], [35]	Easy to implement, applicable for long term data	Increase the noise power
Linear trend subtraction (LTS)	[33], [36]	Good performance, suppress linear amplitude instability	Complex to implement
Singular value decomposition (SVD)	[30]	Increase the SNR	Complex to implement
Dual-frequency radar	[37]	Good performance	Complex radar system

Table 2.2: Comparison between different methods in the literature for stationary clutter removal

2.3. BODY MOVEMENT DETECTION

For the experiments monitoring the vital signs, it is assumed that the human target remains stationary during the measurement period, but it is unnatural to stay stationary for a long period of time, especially for the neonate. Since the proposed processing pipeline is applied to monitor RR and HR when the adults or neonates are in a near-steady state, the initial step is to identify the data segments without large body movement by body movement detection approaches.

Currently, there are various approaches used for detecting body movement. For example, an auto-correlation based technique is applied for detecting body movement during the measurement process with IR-UWB Radar in [38]. For a stationary target, the auto-correlation width is greater than compared to the target with body movement, as there is comparatively less correlation among the signal samples when the target makes

random body movements (RBM). If the correlation width is lower by a certain ratio, then the pipeline can determine that the target is moving and thus stop the estimation of vital signs until the target becomes stationary again.

Moreover, the body movement is detected using the range that maximizes the received signal in [39]. The chest movement due to the vital signs can be considered as a type of micro-motion, so the human target remains in the same range bin. A body movement, e.g., an inadvertent movement of the adult or a change in the position of the neonate during sleep will cause a macro-motion. If this occurs, the human target falls in several range bins. As shown in Eq. 2.7, the range r_m that maximizes the received signal is estimated as:

$$r_m(n_i) = \underset{r}{arg\,max}\, RT[r, n_i], \tag{2.7}$$

where $RT[r,n]$ represents the range-time map, r denotes the index of range bin, n denotes the index of slow time, n_i denotes the i-th chirp. Using a moving window of length L seconds, the sliding standard deviation σ_r is computed:

$$\sigma_r(m) = \sqrt{\frac{1}{L}\cdot\sum_{i=m-L+1}^{m} r^2(i) - (\frac{1}{L}\cdot\sum_{i=m-L+1}^{m} r(i))^2}. \tag{2.8}$$

If the moving deviation is higher than a threshold distance, this segment can be considered as macro-movement by the target, which is the discarded segment.

Additionally, the energy based methods with a customized threshold are applied widely to detect the body movement. In [40], Shang et al. calculate the total energy value for every k data points and compare it with a threshold to determine whether there is a body movement. The Riemann integral of the energy spectrum with a root mean square (RMS) based change point detection method is utilized to determine body movement in [41]. Besides, the Riemann integral of the radar signal amplitude is studied, by Kagawa et al [42], to calculate the body movement index. Last but not least, some approaches are using multiple radars [43], [44], or radar paired with camera [45] to detect or cancel the body movement. To have an overview of the different methods for detecting body movement, Table 2.3 is listed as follows.

Method	**Reference**	**Advantage**	**Disadvantage**
Auto-correlation width	[38]	Easy to implement	Sensitive to noise, low accuracy
Maximum range bin variance	[39]	Easy to implement	Not sensitive for long distance target, unique threshold for different case
Energy based detection	[40], [41], [42]	Easy to implement	Unique threshold for different case
Hybrid radar system	[43], [44], [45]	Good performance	Complex radar system, complex process

Table 2.3: Comparison between different methods in the literature for body movement detection

2.4. RANGE BIN SELECTION

For accurate vital signs monitoring with FMCW radar, a precise selection of the target range bin, where the vital information exists, is crucial. Otherwise, an inappropriate range bin selection can lead to erroneous vital signs monitoring results. With the method used in [46], the range bin that has the maximum average magnitude is selected, by Eq. 2.9, considering the reflected power from the target.

$$r_{selected} = \underset{r}{arg\,max} \left(\frac{1}{n} \cdot \sum_{i=1}^{n} RT[r,n] \right), \tag{2.9}$$

where $RT[r,n]$ represents the range-time map, r denotes the index of range bin, n denotes the index of slow time. This method is easy to implement with good performance, but it can be invalid or inaccurate, when there is body movement. Furthermore, the range bin with the maximum phase variation is chosen in [47], by the expression:

$$r_{selected} = \underset{r}{arg\,max} \left(\sigma_P^2(r) \right), \tag{2.10}$$

where $\sigma_P^2(r)$ represents the variance of the phase information $P(r,n)$ of the range-time map, r denotes the index of range bin, n denotes the index of slow time, but this method is vulnerable to phase noise from the experiment scenario. In [48], instead of selecting one range bin, the range bins within a certain target range are integrated together to be used. However, the vital signs monitoring results may have a low accuracy.

Apart from the traditional methods mentioned above, a novel range bin selection method, that exploits the coherency between the magnitude and phase of the FMCW radar signal is studied in [49] by Choi et al. Because the magnitude and the phase contain the displacement information by the respiration and heartbeat, both the magnitude and the phase need to be used to select the range bin for more accurate vital signs extraction. Since the fluctuation of the magnitude and phase in the range bin where the vital signal exists is highly correlated, a magnitude-phase coherency (MPC) index quantifying the coherency between the magnitude and phase in each range bin, is devised as Eq. 2.11:

$$MPC(r,n) = \frac{\left| \sum_{i=n-n_0}^{n} M(r,n) \cdot P(r,n) \right|}{\sigma_M(r) \cdot \sigma_P(r)}, \tag{2.11}$$

where $M(r,n)$ represents the magnitude value of the range-time map , $\sigma_M(r)$ is the standard deviation of $M(r,n)$. Then the range bin with the maximum MPC index is selected for further processing. Before calculating the MPC index, a bandpass filter is supposed to be applied on the magnitude value and phase information to prevent mutual interference between respiration and heartbeat. To have an overview of the different methods to select the range bin, Table 2.4 is listed as follows.

Method	Reference	Advantage	Disadvantage
Maximum average magnitude	[46]	Good performance, easy to implement	Not applicable for long term data
Maximum phase variation	[47]	Easy to implement	Sensitive to phase noise
Integrate range bins	[48]	Easy to implement	Low accuracy in monitor result
Magnitude-phase coherency (MPC)	[49]	Good performance	Complex process, not sensitive for long distance target

Table 2.4: Comparison between different methods in the literature for range bin selection

2.5. RADAR-BASED VITAL SIGNS ESTIMATION TECHNIQUES

Once the phase information within the selected range bin is obtained, the subsequent step involves applying estimation techniques to this phase information in order to derive the vital signs estimation result. In this section, a comprehensive overview of the current landscape of radar-based vital signs estimation techniques will be presented, not only aiming for neonate, but also adult. One crucial point to clarify is that there are different types of radars, but for now, this section includes all types of radars, without categorization based on radar type or architecture.

As it is described above, the signals due to the vital signs, are low-speed signals with small Doppler shifts and weak echoes. In the meanwhile, heartbeat leads to more feeble chest displacement, thus radar-based RR estimation is more challenging comparing to respiration, usually resulting in lower accuracy. Such inherent characteristic makes these signals susceptible to being lost during the estimation process, especially for neonate's respiration signals, which came from a small size target. Consequently, there must be more effective estimation techniques to detect and extract such signals.

Recently, a study conducted on six neonates to monitor their RR, employing IR-UWB radar owing to its high penetrability and high range resolution, is reported by Kim et al. [6]. The neonate data is categorized into three levels, based on the intensity of body motion. With the help of the Kalman filter (KF) introduced in [38], the RR is estimated for each level's data, while evaluating the performance of radar measurements affected by neonate body movement. Another study conducted by Ji et al. [50], also applies KF to further improve RR estimation quality of adult data. The preliminary experimental results have shown the estimated error is 1.97%-4.26%. One crucial aspect to note with the KF is its sensitivity to model inaccuracies and uncertainties, which may lead to erroneous estimations [51]. In addition, a novel recovery and separation method based on a double parameter least mean square (LMS) filter is developed by He et al. [52]. The obtained results provide evidence that the proposed technique yields more accurate respiration and heartbeat signals when compared to the bandpass filter method and the wavelet transform (WT) method.

Furthermore, in a study conducted by Beltrão et al. [3], a continuous wave (CW) radar is used with a novel random body movement mitigation technique known as non-negative matrix factorization (NMF), which is based on the time frequency decomposi-

tion of the recovered respiration signal. Afterwards, the non-linear least squares (NLS) estimator explained in [53], which explores the harmonic structure of the respiration signal of the neonate, is also employed to achieve an accurate RR estimation. And this study yields promising results, showing the average 10 bpm accuracy for all neonate measurements is higher than 97%. After applying a Butterworth type bandpass filter, a novel peak detection method with power spectrum density (PSD) analysis is employing to obtain RR from a neonate's weak chest vibration with ultra-wide band (UWB) radar in [54]. Since the neonate may move in the crib, a location algorithm is applied periodically to track the current location of the neonate's chest, while the neonate apnea detection is implemented by a dynamic power threshold method. With the same type of radar, the ensemble empirical mode decomposition (EEMD) method and continuous wavelet transform (CWT) that the Morlet wavelet is chosen as the mother wavelet, are used jointly in [55] to improve the SNR, separate vital sign signals and estimate RR and HR of adult.

Another novel approach has been proposed by Khaemphukhiao et al. in [56], which uses a 24 GHz FMCW radar to monitor the RR of the neonates. The mel-frequency cepstral coefficients (MFCCs) are calculated and employed as features for the Gaussian Mixture Model (GMM). This GMM is utilized to identify peaks in the respiration signal, enabling the subsequent estimation of RR for the neonate. The outcomes have an absolute agreement with the standard reference under experimental measurements with a newborn phantom. Unfortunately, it has not been tested in a real clinical setting or the NICU environment. Additionally, an algorithm that deploys Elliptic notch filtering, compressed sensing (CS) based signal reconstruction, and WT is presented in [57], while being proved to be valid for RR and HR estimation by implementing on the neonate dataset of FMCW radar. In [58], a vital sign detection algorithm based on maximum ratio combing (MRC) and variational mode decomposition (VMD) is proposed for multichannel FMCW radar and tested with adult data. The MRC technology is used to combine the multichannel phase signals and improve the SNR of the phase signal, while the VMD algorithm is adopted to decompose the combined phase signal. Then the resulting intrinsic mode functions (IMFs) are used to reconstruct the respiration and heartbeat signals accurately.

Not only the novel techniques which have complex computational, but also the conventional radar-based techniques, such as fast Fourier transform (FFT) and STFT, have been utilized in the monitoring of RR for adult as well. In the study reported by Alizadeh et al. [47], an FMCW radar is utilized in a bedroom environment to extract the RR and HR of an adult target lying on a bed. Two rounds of FFT are utilized in the process. The initial FFT is employed to generate range-time information, while the second FFT is applied to estimate the RR and HR within the specified range profile. This approach leads to a significant 94% correlation between the estimation obtained from the radar and ground truth from the reference sensor. Besides, another estimation method based on FFT, called multifold high order cumulant fast Fourier transform (MHOC-FFT) is conducted with Cramer-Rao Lower Bound (CRLB) in [36], to process the data of simulated noisy signal and to estimate RR. By using the FFT and adaptive peak detection in [59], the relative error of the HR estimation is proved larger compared to the RR, but it is still within a reasonable range.

Moreover, a dataset of 16 volunteers is acquired with three different radars, two FMCW

radars and one pulsed coherent (PC) radar in [60], yielding a total of 400 minutes of radar-recorded vital sign data. Afterwards, the dataset is processed by four processing algorithms, two of which are FFT based algorithms, while the other two are STFT based. And this work proves that it is possible to measure RR and HR with all the radars analysed, and the best performing algorithm varies on the radar used. Moreover, no correlation are founded between the power consumption of the radar and the accuracy of the estimation. Besides, a remote vital signs monitoring method is discussed in [61], which implements a STFT based algorithm and a wavelet filter to achieve a real-time RR and HR estimation of adult with CW radar. Beyond those, there are other vital signs estimation techniques, such as parameterized demodulation (PD) [62], multiple signal classification (MUSIC) [63], [64], recursive least squares (RLS) [65] and so on. Overall, a summary of the vital signs estimation techniques mentioned in this section, is shown in Table 2.5, 2.6.

2.6. SUMMARY

This chapter firstly introduces the mathematical signal models for cardiopulmonary activity, formed by two components, the respiration model and the heartbeat model. As for the radar response for the signal model, it will be described in Chapter 4. The remaining parts of the literature review present and discuss the state of art about the main processing steps, which are commonly used in the vital signs monitoring pipelines, including:

- The stationary clutter removal part, where the unwanted static echos of the received signal are eliminated. This process enhances the clarity of the signal associated with chest movement, making it more distinguishable in the range-time map.
- The body movement detection part, which enables the identification of body movement of the target. This process allows for the selection of data segments during near-steady conditions for subsequent processing.
- The range bin selection part, which enables the identification of the specific range bin where vital sign information is present. This process ensures that as much vital sign information as possible will is utilized for the pipeline.
- The radar-based vital signs estimation techniques part, which provides the techniques used to effectively estimate RR and HR as final results. This process improves the accuracy of the vital signs monitoring.

Based on the content of this chapter, the proposed vital signs monitoring pipeline is designed by choosing methods or techniques described in here.

Reference	Radar type	Vital sign	Target	Distance and orientation to radar	Algorithm\method
Beltrão et al. [3]	24 GHz CW radar	Respiration	Neonate	45 - 50 cm Front side and left side for single/twins cases	NLS, NMF
Kim et al. [6]	7.29 GHz IR-UWB radar	Respiration	Neonate	35 cm Front side	KF
Khan et al. [38]	6.8 GHz IR-UWB radar	Respiration Heartbeat	Adult	100 - 200 cm Front side and back side	KF
Alizadeh et al. [47]	77 GHz FMCW radar	Respiration Heartbeat	Adult	170 - 180 cm Front side	FFT
Ji et al. [50]	77 GHz FMCW radar	Heartbeat	Adult	50 cm Front side	KF
He et al. [52]	FMCW radar	Respiration Heartbeat	Simulation	200 - 300 cm Front side	LMS, WT
Beltrão et al. [53]	77 GHz FMCW radar	Respiration	Adult Neonate	150 cm Front side	NLS
Huang et al. [54]	UWB radar	Respiration	Neonate	100 cm Front side	Butterworth bandpass filter, peak detection
Hu et al. [55]	6.8 GHz IR-UWB Radar	Respiration Heartbeat	Adult Neonate	20 - 300 cm Front side	EEMD, CWT
Khaemphukhiao et al. [56]	24 GHz FMCW radar	Respiration	Neonate	35 cm Front side	MFCCs, GMM
Tekleab et al. [57]	60 GHz FMCW radar	Respiration Heartbeat	Neonate	N/A	Elliptic notch filtering, CS, WT
Qu et al. [58]	24 GHz FMCW radar	Respiration Heartbeat	Adult	40 cm Front side	MRC, VMD

Table 2.5: Summary of vital signs estimation techniques (part 1)

Reference	Radar type	Vital sign	Target	Distance and orientation to radar	Algorithm\method
Wang et al. [59]	80 GHz FMCW radar	Respiration Heartbeat	Adult	Front side, back side, left side 100 - 200 cm	FFT, peak detection
Giordano et al. [60]	60/80 GHz FMCW radar 60 Ghz PCR radar	Heartbeat	Adult	45 - 55 cm Front side	FFT, STFT
Hu et al. [61]	24 GHz CW radar	Respiration Heartbeat	Adult	50 cm Front side	STFT
Xiong et al. [62]	10.525 GHz CW radar	Respiration Heartbeat	Adult	100 - 150 cm Front side	PD
Le Kernec et al. [63]	24 GHz FMCW radar	Respiration Heartbeat	Adult	200 cm Front side	MUSIC
Sun et al. [64]	2.475 GHz CW radar	Respiration Heart beat	Adult	100 - 300 cm Front side	MUSIC
Huang et al. [65]	77 GHz FMCW radar	Heartbeat	Adult	30 - 70 cm Front side	RLS

Table 2.6: Summary of vital signs estimation techniques (part 2)

3

PROCESSING PIPELINE OF VITAL SIGNS MONITORING

This chapter gives a view of the proposed processing pipeline for monitoring the vital signs of the target by presenting examples of real data processing. In Section 3.1, the overview of the proposed processing pipeline is described. After that, the pre-process part of the pipeline is introduced in Section 3.2. The data segment selection based on body movement detection and the range bin selection are presented in Section 3.3 and Section 3.4 respectively. Next, the approach used to estimate RR and HR is introduced in Section 3.5. The procedure of processing and analysing the estimation results statistically is described in Section 3.6. Last but not least, a summary of the proposed processing pipeline is presented in Section 3.7.

3.1. PIPELINE OVERVIEW

The aim of the project is to monitor the vital signs of the neonates, which are RR and HR, with the proposed processing pipeline presented in Figure 3.1. For this pipeline, it begins with the raw data which contains the vital signs information collected by the FMCW radar. After applying FFT and pre-process approaches, the range-time map is generated to identify the target data segments and select relevant range bins. The next step is unwrapping the phase for the purpose of implementing the bandpass filter and the STFT algorithm. In order to estimate RR and HR, a peak detection approach is applied to the spectrogram derived from the STFT algorithm. Subsequently, estimation results are compared with the ground truth and statistical analysis is performed by calculating statistical parameters and drawing the correlation graph and the Bland-Altman plot. The details of each procedure will be described by presenting examples of real data processing in the following sections.

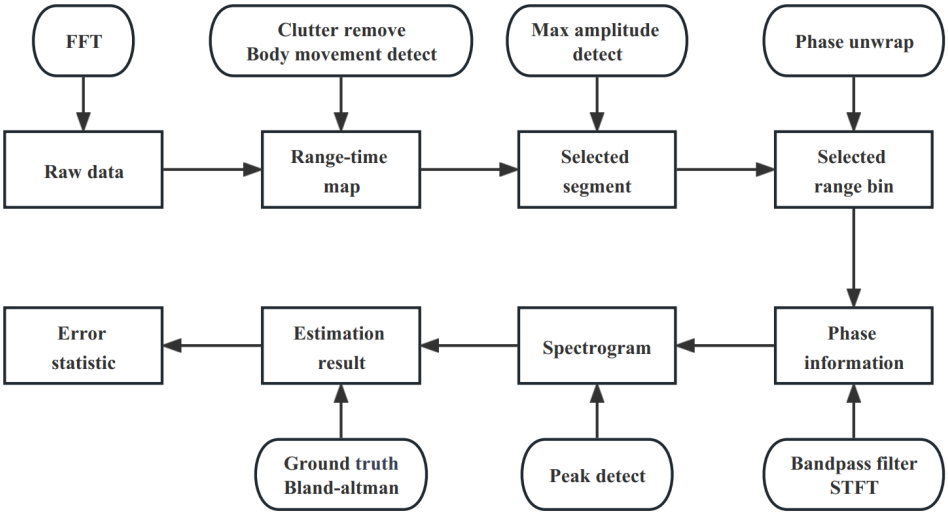

Figure 3.1: Overview of the proposed processing pipeline for vital signs monitoring, where the square blocks indicate the data format or structure and the oval blocks indicate the processing step or technique applied

3.2. PRE-PROCESS

Before detecting the body movement and identifying the target data segments for further processing, it is necessary to generate the range-time map based on the raw data and remove the clutter from the range-time map, which are regarded as pro-process in the proposed processing pipeline.

The raw data of the FMCW radar consists of stacked in-phase and quadrature components of each chirp. Therefore, it is necessary to sample the beat signal into each chirp and stack in rows, a raw data matrix $D[\tau, t]$ can be built, with τ being the number of samples per chirp over fast time and t being the number of chirps over slow time. Subsequently, a FFT is applied on each row of the $D[\tau, t]$ matrix, resulting in the range-time map $RT[r, n]$, where r represents the index of range bin over fast time, n represents the index of chirp over slow time. Two range-time maps based on the real data of adult and neonate are shown in Figure 3.2(a) and Figure 3.2(b).

As mentioned in the previous chapter, the range-time map described above contains stationary clutter that needs to be eliminated before detecting body movement. For the purpose of high computing efficiency and easy implementation while ensuring good performance, the MS method is chosen. Due to the long-term monitoring of the neonate dataset which may span over an hour, the stationary clutter is not static throughout this period. Therefore, the MS method requires a windowing process to handle the changing of the stationary clutter. To solve this problem, the range-time map $RT[r, n]$ is divided into segments with a duration of 10 seconds, over slow time dimension. For each segment, the MS method is implemented to remove stationary clutter periodically, and Figure 3.2(c) and Figure 3.2(d) show the results of the same real data after MS method.

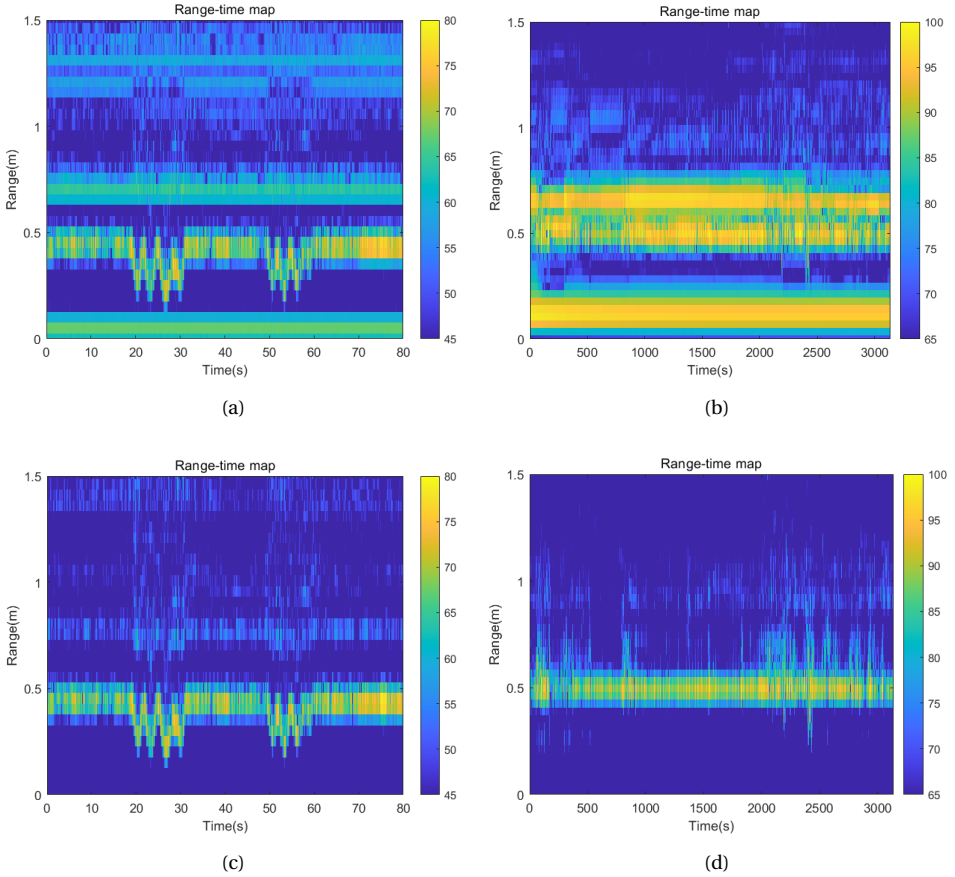

Figure 3.2: Range-time maps based on the raw data of the 60 GHz FMCW radar: (a) range-time map of adult data; (b) range-time map of neonate data; (c) range-time map of adult data after MS method; (d) range-time map of neonate data after MS method

3.3. DATA SEGMENT SELECTION

After the pre-process section, the next step involves detecting the data segments that contain the body movement of the target and discarding those segments. The rest of the data segments are the ideal part for further processing, where the target is in a near-steady state. According to Table 2.3, the auto-correlation width method is sensitive to noise, so it is not suitable for neonate monitoring, which must be affected by ambient noise. Due to the fact that only one radar is used to monitor vital signs in this thesis project, the hybrid radar system method is also excluded. Since the energy based detection method is also applicable for long distance target, it is chosen to detect the body movement and select the data segment.

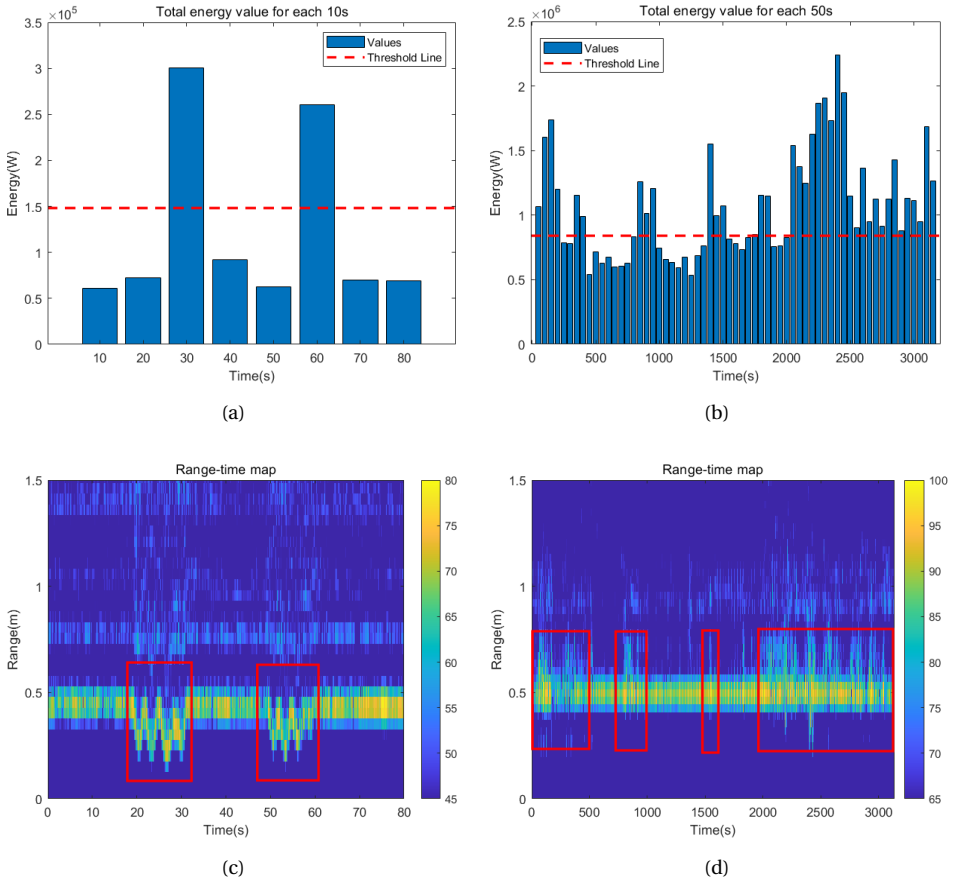

Figure 3.3: Bar graphs of total energy value for each k chirps and discarded segments: (a) bar graph of adult data with an interval of 10s; (b) bar graphs of neonate data with an interval of 50s; (c) discarded segments of adult data due to high energy associated to large body movements (in red); (d) discarded segments of neonate data due to high energy associated to large body movements (in red)

With the range-time map, the target position can be distinguished, for example the adult is in the range bin cells of 0.3 - 0.7 m as shown in Figure 3.2(c). After obtaining the position of the target, the energy of the signal attributed to vital signs for each chirp can be calculated, by summing the amplitude of the range bin cells where the target is located. Subsequently, the next step is to calculate the total energy value for every k chirps, and those total energy values are listed in the bar graph to compare with a threshold and determine whether there is a body movement, as shown in Figure 3.3(a), 3.3(b). If the total energy value exceeds the threshold, it indicates the presence of significant body movement during the period of those k chirps. Then those segments will be discarded, which are pointed out with the red blocks in Figure 3.3(c), 3.3(d). Here in the adult measurement case, k equals to the number of chirps in 10 seconds, while k equals to the number of chirps in 50 seconds in the neonate measurement case, because of the

long-term monitoring for the neonate which may span over an hour. As for the threshold, different cases require different thresholds, which can be calculated based on a large number of tests.

3.4. RANGE BIN SELECTION

With the selected data segments, the range bin, which is the most relevant to the vital signs, is supposed to be selected for further RR and HR estimation. Based on Table 2.4, the integrate range bins method will result in low accuracy of the vital signs monitor result, so this method is discarded. The remaining three methods are evaluated through processing real data segments.

During the real data segment processing, each method processes the real data to select a range bin as a result. The selected range bin is then compared with the manually selected range bin, which serves as the ground truth. After processing multiple data segments, the method that produces a result closest to the ground truth will be selected. For each data segment, the candidate of the range bins will be selected based on the possible positions of the target. A 5 seconds sliding window is used as a time frame to calculate the corresponding range bins of the three methods, based on the Eq. 2.9, 2.10 and 2.11, and the range bins will be considered as the results at that specific moment. Therefore, a graph, which shows the range bin selection of each second for this segment, can be drawn as shown in Figure 3.4(b). The next step is to calculate the mean of the range bins over the whole duration of the segment for each method, which is the selected range bin for this segment. Here, for the example segment, the range bin results are 0.50 m, 0.45 m, and 0.55 m respectively, while the manually selected range bin is 0.50 m.

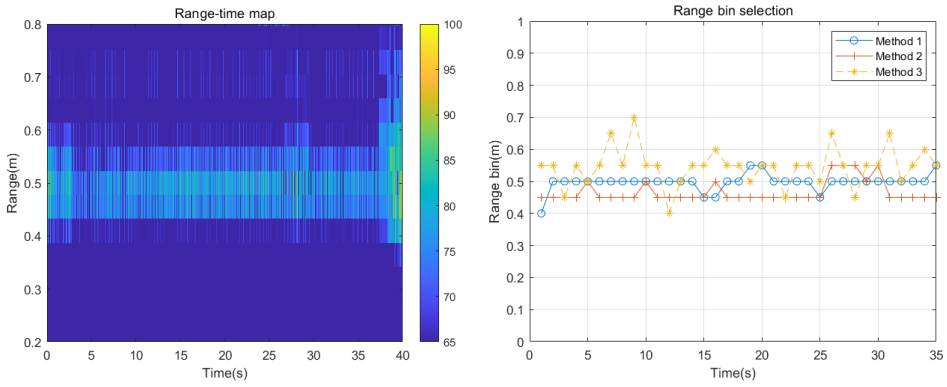

(a) (b)

Figure 3.4: Range bin selection example: (a) range-time map of the example segment of data, where the target occupies multiple range bins; (b) range bin selection of each second for the example segment by applying different methods

In this case, 8 different data segments have been processed as described above, of which half are adult data, and the other half are neonate data. The results are listed in

Table 3.1, where M1 is the result of the maximum average magnitude method, M2 is the result of the maximum phase variation method and M3 is the result of the MPC method. It is clear that the maximum average magnitude method performs well. Besides, the maximum phase variation method works better for the adult data, since the neonate data may have more phase noise. And the mutual interference between respiration and heartbeat signal may be the cause of the maximum error in the MPC method. Therefore, the maximum average magnitude method is chosen for the proposed processing pipeline.

Segment No.	**Segment duration [s]**	**M1 [m]**	**M2 [m]**	**M3 [m]**	**Ground truth [m]**
1	40	0.50	0.45	0.55	0.50
2	50	0.50	0.55	0.60	0.50
3	70	0.45	0.30	0.40	0.45
4	70	0.60	0.60	0.60	0.60
5	200	0.58	0.46	0.54	0.58
6	250	0.42	0.38	0.58	0.46
7	300	0.50	0.62	0.58	0.50
8	400	0.42	0.46	0.26	0.38

Table 3.1: Example of range bin selection results with different methods M1-M3 for the 8 different data segments, 1-4 are adult data, 5-8 are neonate data

3.5. RESPIRATION RATE AND HEARTBEAT RATE ESTIMATION

With the selected data segments and corresponding range bins, the next step is to unwrap the phase to gather the phase information in the range bin. Afterwards, the bandpass filter is implemented to minimize the interaction between respiration and heartbeat. And the boundary of the bandpass filter is based on Table 2.1. Then, the STFT algorithm will process the data coming out of the bandpass filter, to get the spectrogram, as shown in Figure 3.5, with a 0.2-0.8 Hz bandpass filter for RR and a 1-1.8 Hz bandpass filter for HR. In order to estimate RR and HR, a peak detection is implemented on each column of the spectrogram over slow time.

After having the estimation results of both RR and HR, two types of error, the absolute error e_{abs} and the relative error e_{rel} can be calculated for each measurement point by:

$$\begin{aligned} e_{abs} &= abs(a-b), \\ e_{rel} &= \frac{abs(a-b)}{b} \cdot 100\%, \end{aligned} \tag{3.1}$$

where a represents the estimated value and b represents the ground truth value. As shown in Figure 3.6, the estimate value and ground truth, with the calculated errors can be drawn. It is important to highlight that the presence of the apnea state can be effectively detected through the application of the threshold method, as shown in Figure 3.5(a). Between 50-70 s, the target is in the state of apnea and the threshold is set as 60 dB. Since the peak values in that period are lower than the threshold, the period is considered as apnea. Regarding the threshold value, it is not fixed and can be adjusted to

suit the specific conditions of each unique circumstance, based on the tests conducted in that particular situation. For instance, the threshold value is set at 80% of the mean value of peak detected values in this case.

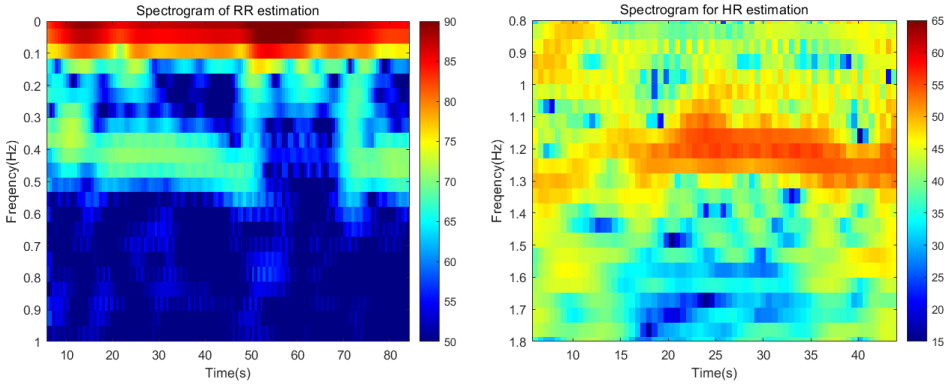

(a) (b)

Figure 3.5: Spectrogram examples: (a) spectrogram for RR estimation; (b) spectrogram for HR estimation

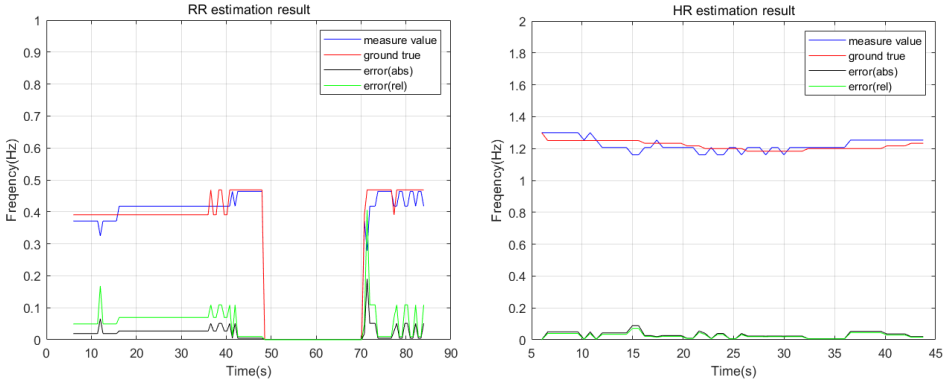

(a) (b)

Figure 3.6: Estimation result examples based on the spectrograms shown in Figure 3.5: (a) RR estimation result; (b) HR estimation result

3.6. RESULT STATISTICS

After having the values of two types of error for both RR and HR, the properties of the errors, including the maximum error, the minimum error, the mean of the error, and the standard deviation of the error, will be calculated and listed in a table to evaluate the performance of the pipeline, as shown in Table 3.2. Moreover, to gain a deeper understanding of the estimation results, two graphical representations are generated, as shown in

Figure 3.7. The first is a correlation graph, displaying the slope-intercept equation, the square of Pearson correlation coefficient (PCC), and the number of measurement points. Another is a Bland-Altman plot that shows the reproducibility coefficient (RPC), the coefficient of variation (CV), and the Limits of Agreement (LoA).

Property of error	Type of error	Respiration rate	Heartbeat rate
Maximum	Absolute [Hz]	0.211	0.282
	Relative [%]	40.6	22.5
Minimum	Absolute [Hz]	0	0
	Relative [%]	0	0
Mean	Absolute [Hz]	0.028	0.081
	Relative [%]	5.7	6.5
Standard deviation	Absolute [Hz]	0.031	0.051
	Relative [%]	5.4	4.2

Table 3.2: Example table of error properties, giving statistical properties to analyse the error in the estimation of vital signs of a data segment

The correlation graph provides a visual representation of the relationship between the estimation results and the ground truth. Besides, it includes the slope-intercept equation, which indicates the slope and intercept of the linear regression line fitted to the data points. Additionally, the squared of PCC reflects the strength of the linear relationship between the estimation results and ground truth, which can be calculated by:

$$PCC = \frac{1}{n-1}\sum_{i=1}^{n}\left(\frac{R_i-\mu_R}{\sigma_R}\right)\left(\frac{G_i-\mu_G}{\sigma_G}\right), \tag{3.2}$$

where R represents the matrix of radar measured values, G represents the matrix of ground truth values, μ and σ represent the mean and standard deviation respectively, n represents the number of measurement points, which is also shown in the graph to indicate the sample size used for the correlation analysis [47].

On the other hand, the Bland-Altman plot offers insights into the agreement and consistency between the radar estimation results and the ground truth. As for the RPC, it is represented as a value and a percentage, which can be calculated by:

$$\begin{aligned} RPC_{val} &= 1.96 \cdot std(D), \\ RPC_{per} &= 1.96 \cdot std\left(\frac{D}{mean(R,G)}\right) \cdot 100\%, \end{aligned} \tag{3.3}$$

where D is the matrix of the difference values between the radar measured values and the ground truth values [66]. By presenting RPC, the reproducibility and consistency between the estimation results and ground truth is assessed. Furthermore, another important parameter, CV can be calculated by:

$$CV = \frac{std(D)}{mean(\frac{R+G}{2})} \cdot 100\%, \tag{3.4}$$

is displayed, providing information about the relative variability and dispersion between the estimation results and ground truth [66]. As for the LoA, it can be calculated by:

$$LoA = mean(D) \pm 1.96 \cdot std(D), \tag{3.5}$$

which statistically assesses the agreement between the radar estimation results and the ground truth [67].

After obtaining an overall perspective of the estimation results, a bar graph illustrating the absolute error properties for each measured target is generated, as shown in Figure 3.8, which allows for a detailed analysis of each individual target.

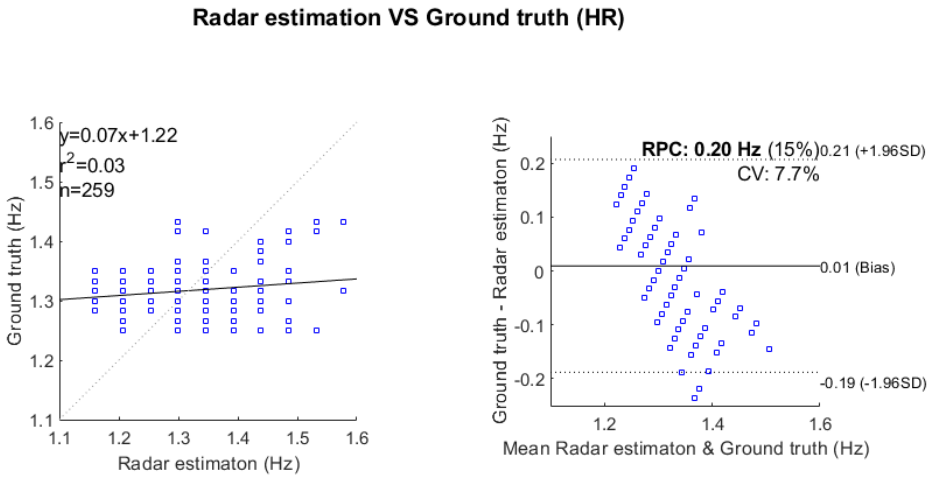

Figure 3.7: Example correlation graph and Bland-Altman plot, showing the relation between the estimation results and ground truth

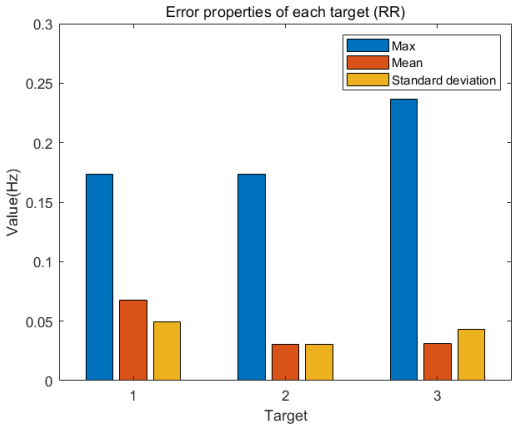

Figure 3.8: Example bar graph, showing the absolute error properties for each measured target

3.7. SUMMARY

This chapter presents the proposed processing pipeline for monitoring the vital signs of a target, using real data processing examples for illustration. The overview of the pipeline is described in Figure 3.1, providing the outline of the entire process. Based on the procedure of the pipeline, important information is pointed out as follows:

- For the clutter removal, the MS method is chosen, because of high computing efficiency and good performance. Since the long-term monitoring of the neonate dataset and the stationary clutter may not be static throughout this period, the MS method is applied with a sliding window.
- The energy based detection method is applied with the threshold method to detect body movement and select data segments, meaning if the total energy of the segment exceeds the threshold, it will be considered as body movement.
- Three range bin selection methods, including maximum average magnitude method, maximum phase variation method, and MPC method, are evaluated by applying them to real data segments. Based on the results in Table 3.1, the maximum average magnitude method has the best performance, so that it is utilized in the pipeline.
- As for the process of RR and HR estimation, it is mainly based on the STFT algorithm with peak detection of each column of the spectrogram, which enables a better understanding of a signal's time and frequency characteristics while being respond promptly to achieve real-time monitoring.
- The result statistics part Section 3.6 analyses the estimation result and evaluates pipeline performance with the help of an error property table, a correlation graph, a Bland-Altman plot, and a bar graph, which give an overall perspective of the estimation result and individual analysis of each target.

4

SIMULATIONS AND VALIDATION

In this chapter, the validation of the proposed processing pipeline is carried out by using simulations of vital signs based on the mathematical model. Besides, a Monte Carlo test is implemented to evaluate the pipeline. Section 4.1 focuses on the radar response of the cardiopulmonary activity based on the mathematical signal model described in Chapter 2. The Monte Carlo test and the selection of the window size as well as the overlap time for the STFT algorithm are discussed in Section 4.2. Besides, to assess the pipeline's effectiveness, the Monte Carlo test is performed using the chosen window size and overlap time. At the end of this chapter, a summary of the simulation work is shown in Section 4.3.

4.1. RADAR RESPONSE OF THE CARDIOPULMONARY ACTIVITY

Considering the mathematical signal model for cardiopulmonary activity in Chapter 2 and the derivations done by Su et al. in [68], [69], the position of the monitoring target at a distance R_0 from the radar, the chest movement $R(t)$ can be expressed as:

$$\begin{aligned} R(t) &= R_0 + R_r(t) + R_h(t) \\ &= R_0 + \frac{\alpha_r}{2} \cdot \left(1 - \cos\left(2\pi f_r \cdot t\right)\right) + \alpha_h \cdot \cos\left(2\pi f_h \cdot t\right), \end{aligned} \tag{4.1}$$

where assuming the cardiopulmonary activity has constant amplitude. Here the description of the chest movement is simply by summing Eq. 2.1 and Eq. 2.4 together, as shown in Figure 4.1, but the real model is more complex as respiration and heartbeat can modulate each other. Afterwards, the phase history $\varphi_{ph}(t)$ over slow time can be written as:

$$\begin{aligned} \varphi_{ph} &= \frac{4\pi f_c}{c} \cdot R(t) \\ &= \frac{4\pi f_c}{c} \cdot \left[R_0 + \frac{\alpha_r}{2} \cdot \left(1 - \cos\left(2\pi f_r \cdot t\right)\right) + \alpha_h \cdot \cos\left(2\pi f_h \cdot t\right)\right], \end{aligned} \tag{4.2}$$

where f_c represents the carrier frequency of the radar, c represents the speed of the light. An extra phase φ_e due to the wrapped phase caused by R_0 is considered, and it can be

expressed as:

$$\varphi_e = wrap\left[\frac{4\pi f_c}{c}\cdot R_0\right]. \tag{4.3}$$

Therefore, the phase history becomes:

$$\begin{aligned}\varphi_{ph} &= \frac{4\pi f_c}{c}\cdot R(t)\\ &= \varphi_e + \frac{4\pi f_c}{c}\cdot\left[\frac{\alpha_r}{2}\cdot\left(1-\cos\left(2\pi f_r\cdot t\right)\right)+\alpha_h\cdot\cos\left(2\pi f_h\cdot t\right)\right],\end{aligned} \tag{4.4}$$

And the range history over slow time can be recovered from the phase history of the beat signal as:

$$R(t) = \frac{\varphi_{ph}(t)c}{4\pi f_c}. \tag{4.5}$$

Finally, with the phase history, the beat signal over slow time, can be written as:

$$s(t) = A\cdot exp(j\varphi_e)\cdot exp(j\frac{4\pi f_c}{c}\cdot\left[\frac{\alpha_r}{2}\cdot\left(1-\cos\left(2\pi f_r\cdot t\right)\right)+\alpha_h\cdot\cos\left(2\pi f_h\cdot t\right)\right]), \tag{4.6}$$

where A is the amplitude of the processed signal.

From that information, the radar response of the cardiopulmonary activity is described by equations Eq. 4.1 - Eq. 4.6, which can be used for the simulate the chest movement and extract the phase information contained in the beat signal. Assuming that the beat signal is sampled for each chirp with τ samples and stacked in columns, a raw data matrix $D[\tau, t]$ can be built, with τ being the index of samples per chirp over fast time and t being the index of chirps over slow time. The subsequent phase of the simulation work follows the same steps as illustrated in the pipeline. For the sake of simplicity, there is no stationary clutter and body movement simulated in the simulation work.

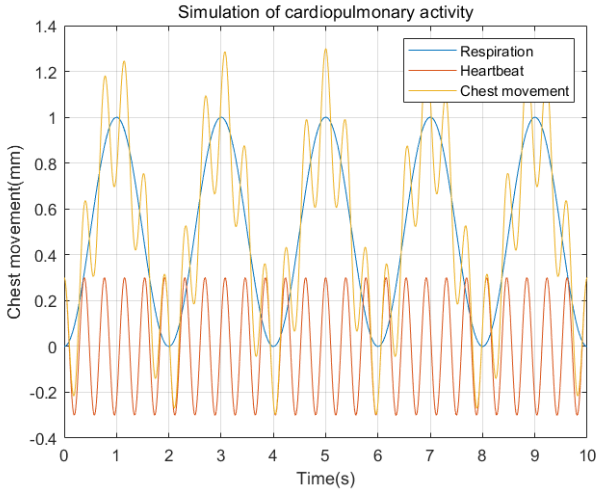

Figure 4.1: Chest movement due to cardiopulmonary activity, simulated using the mathematical model described in Chapter 2

4.2. SIMULATION AND MONTE CARLO TEST

The simulation work and evaluation process are mainly based on the Monte Carlo test. In the Monte Carlo test, random parameters or settings are generated with a specified probability distribution, and these random parameters or settings will be used to simulate the behavior of the proposed processing pipeline as described in Chapter 3. By running multiple simulations with different random inputs, a statistical analysis can be conducted to evaluate the performance of the proposed processing pipeline.

4.2.1. MONTE CARLO TEST

With the Eq. 2.1 and Eq. 2.4 to describe the cardiopulmonary activity, the next step is to modify the respiration frequency f_r and the heartbeat frequency f_h in those equations. Therefore, in the Monte Carlo test, there are three different inputs that can be changed randomly, including the frequency step, the time scale, and the waveform. As shown in Figure 4.2, taking the respiration frequency as an example, the frequency step (indicated with green mark) and the time scale (indicated with red mark) of the waveform can be randomly varied within the defined scales in Table 2.1.

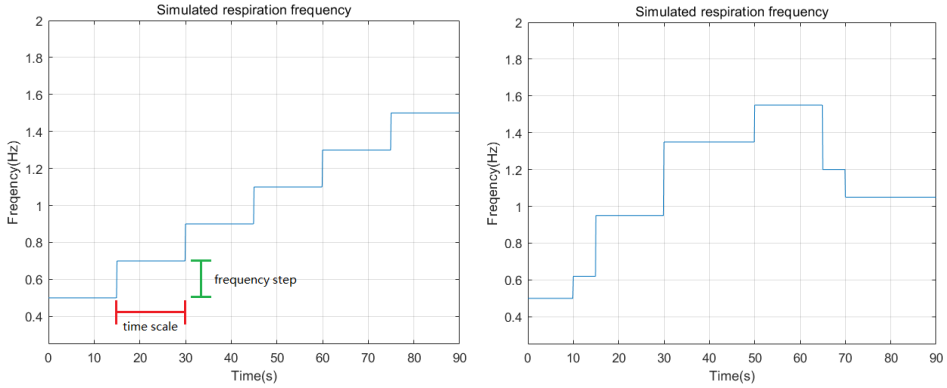

(a) (b)

Figure 4.2: Example of respiration frequency waveforms which change the frequency step and the time scale: (a) frequency step and time scale in a defined pattern; (b) after frequency step and time scale changing randomly to define another different pattern

Additionally, three different waveforms can be randomly selected to simulate the patterns of respiration and heartbeat, as shown in Figure 4.3. One is simulating the respiration frequency increasing first, going down slowly, and staying stable in the end. Another is the respiration frequency increasing first and suddenly going down to a certain value. The last one is simulating irregular rapid changes in respiratory frequency, which is the most critical pattern to test the pipeline. Besides, for each simulated data segment, the duration is 90 seconds. Then, by conducting multiple simulations with different combinations of these inputs, a comprehensive Monte Carlo test is applied to assess the proposed processing pipeline, which also can be used to help with the selection of the

window size and the overlap time for STFT.

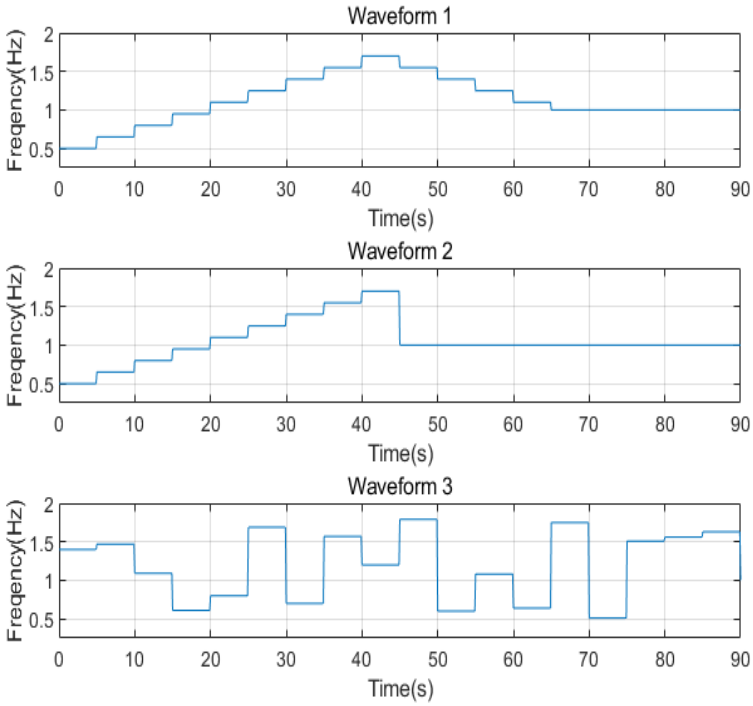

Figure 4.3: Different respiration frequency waveforms: waveform 1, frequency goes up and goes down slowly; waveform 2, frequency goes up and suddenly goes down; waveform 3, frequency with irregular rapidly changes

4.2.2. WINDOW SIZE SELECTION

In the context of STFT, the window size refers to the length of the window function applied to the signal in the time domain. The window function is used to divide the signal into shorter segments, and the size of this window determines the length of each segment for which the FT will be applied. The choice of window size affects the trade-off between time and frequency resolution in the STFT analysis. Smaller window sizes provide higher time resolution but lower frequency resolution, while larger window sizes offer higher frequency resolution but lower time resolution. Therefore, selecting an appropriate window size is important to achieve the desired balance between these two aspects for specific signal analysis.

The window size selection for STFT is conducted with the help of the Monte Carlo test. The window size is set from 1 second to 15 seconds, with a 1 second increment. And for each window size, one Monte Carlo test is conducted to record the absolute error as shown in Eq. 3.1, which will be used to calculate the properties of the absolute error, including the maximum error value, the minimum error value, the mean value and the standard deviation value of the error. With those properties, Figure 4.4 is drawn, which indicates that the estimation performance becomes better with the increasing of

the window size in the case of the window size less than or equal to about 6 seconds. After the window size is larger than 6 seconds, the estimation performance has not changed significantly, only the maximum error value is decreasing. Considering the frequency resolution of the STFT, the window size is set at 12 seconds, which can achieve a frequency resolution of approximately 0.08 Hz, with a relatively small maximum error.

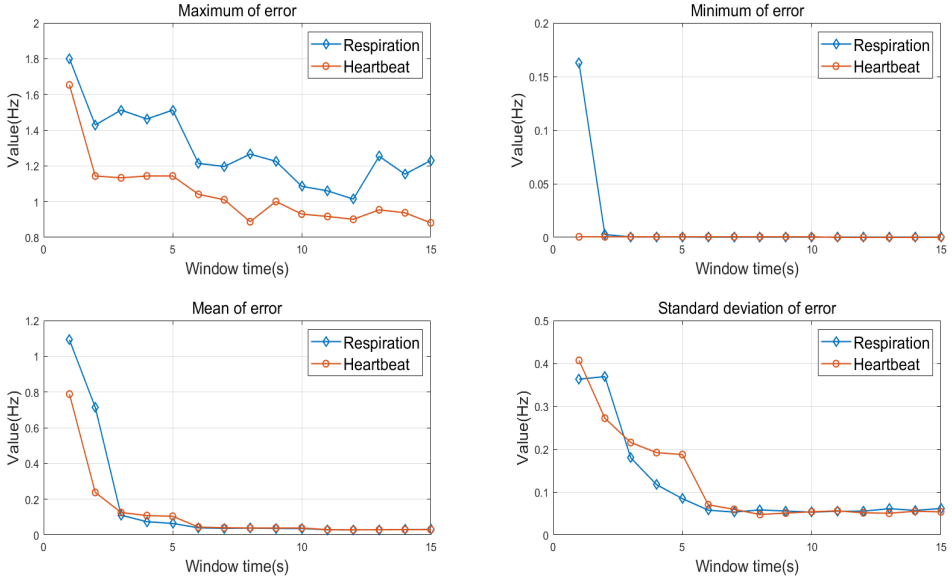

Figure 4.4: Comparison of the pipeline performance with different window size, where the four sub-figures show the changing of the error properties with different window sizes from 1 second to 15 seconds, with a interval of 1 second

4.2.3. OVERLAP TIME SELECTION

For the STFT, the overlap time refers to the amount of time by which consecutive windows overlap during the analysis. It is a crucial parameter that determines how much information from adjacent segments is shared during the STFT computation. Choosing an appropriate overlap time is important as it also affects the trade-off between time and frequency resolution. A larger overlap time improves time resolution but may introduce frequency domain redundancy, reducing frequency resolution. Conversely, a smaller overlap time enhances frequency resolution but may result in less smooth time-domain representations of the signal and reduced time resolution.

The overlap time selection for STFT is also conducted with the help of the Monte Carlo test. The overlap time is set from 5% to 95%, with a 5% increment. And for each overlap time, one Monte Carlo test is conducted to record the absolute error as shown in Eq. 3.1, which will be used to calculate the same properties of the absolute error as described in the previous section. With those properties, Figure 4.4 is drawn and it shows that the estimation performance has not changed significantly with the increasing of

overlap time, only the maximum error has a quite slight upward trend. As a result, it can be concluded that the overlap time rarely affects estimation performance directly. Considering the time resolution of the STFT, the overlap time is set at 95%, which can ensure that there will be at least one measurement point per second in the spectrogram.

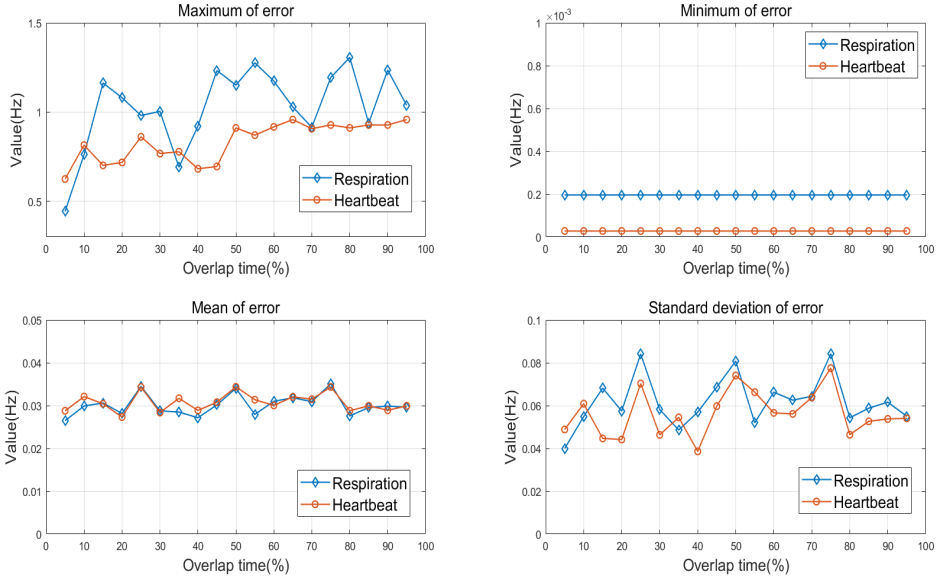

Figure 4.5: Comparison of the pipeline performance with different overlap time, where the four sub-figures show the changing of the error properties with different overlap times from 5% to 95%, with a interval of 5%

4.2.4. SIMULATION RESULTS

With the selected window size and overlap time for STFT, the Monte Carlo test, which has three randomly changing inputs as described in Section 4.2.1, is conducted again. For this Monte Carlo test, there are two hundred simulated data segments with the randomly changing waveforms evaluated to generate overall simulation results. Based on the simulation results, the properties of the absolute error and the relative error are presented in Table 4.1.

For the estimation of RR, the absolute error ranges from 0 to 1.073 Hz, while the range spans from 0% to 178.5% in terms of relative error. However, such high maximum errors do not necessarily indicate poor performance of the pipeline. It is important to note that the maximum errors represent extreme cases, which is only a small subset of measurement points, and can be distinguished from the correlation graph and the Bland-Altman plot shown in Figure 4.6, 4.7. With an average error of 0.029 Hz or 2.8% and a standard deviation of 0.053 Hz or 5.6%, it indicates the majority of the measurement points are accurate and the errors are relatively stable and tightly clustered around the mean value.

Same to the RR estimation, the absolute error of HR estimation varies from 0 to 0.916 Hz. While the values of relative error range from 0% to 43.6%, which is quite small com-

pared to RR estimation, due to the fact that the ground truth of HR can be even times larger than RR. For the same reason, the approximately same average and standard deviation of the absolute error compared to RR, leads to much lower values for relative error in HR estimation.

Property of error	Type of error	Respiration rate	Heartbeat rate
Maximum	Absolute [Hz]	1.073	0.916
	Relative [%]	178.5	43.6
Minimum	Absolute [Hz]	0	0
	Relative [%]	0	0
Mean	Absolute [Hz]	0.029	0.029
	Relative [%]	2.8	1.2
Standard deviation	Absolute [Hz]	0.053	0.051
	Relative [%]	5.6	2.1

Table 4.1: Error properties of simulation result, where two hundred simulated data segments with randomly changing waveforms are evaluated

With high values of the squared PCC over 13700 measurement points, there is a strong positive linear correlation between the estimation results and the ground truth for both RR and HR. Besides, 5.3% and 2.4% CV values for RR and HR respectively show the measurement points are relatively close to the mean level with a low variability. And there are approximately 96% for RR and HR measurement points in the region of LoA, with an absolute error lower than 0.12 Hz. Last but not least, such low RPC values indicate satisfactory reproducibility and agreement between estimation results and the ground truth for both RR and HR.

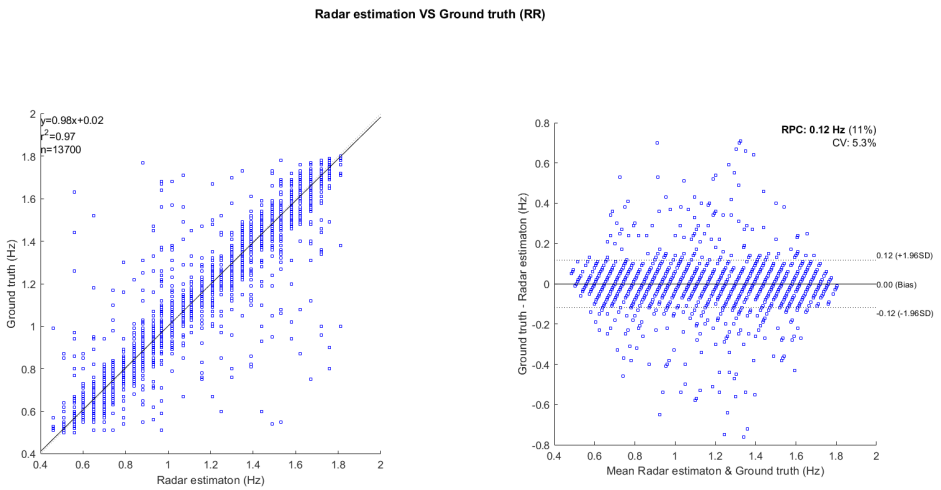

Figure 4.6: Correlation graph and Bland-Altman plot of RR estimation, showing the relation between the estimation results and ground truth (simulation result)

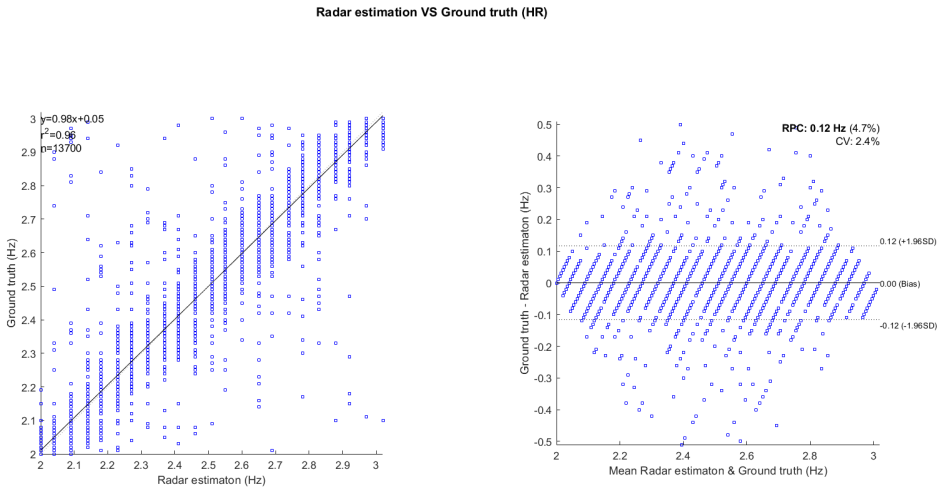

Figure 4.7: Correlation graph and Bland-Altman plot of HR estimation, showing the relation between the estimation results and ground truth (simulation result)

4.3. SUMMARY

This chapter introduces the radar response of cardiopulmonary activity with equations, which can be used to simulate the raw data from the radar. Based on the simulated raw data, the validation of the pipeline is also discussed with a Monte Carlo test, which has three random inputs, including the frequency step, the time scale, and the waveform, in order to simulate different vital signs patterns of different people. With the help of the Monte Carlo test, the window size and the overlap time of the STFT algorithm are set at 12 seconds and 95% respectively.

Additionally, another Monte Carlo test with the three randomly changing inputs as described in Section 4.2.1, is conducted based on the selected window size and overlap time for STFT to get overall simulation results. Finally, to assess and validate the pipeline, the Table 4.1 about properties of error, correlation graphs, and Bland-Altman plots shown in Figure 4.6, 4.7 are generated demonstrating:

- For both RR and HR, the minimum error for both types is zero, while the mean and the standard deviation stay at an extremely low level. It should be noted that a high maximum relative error does not mean a poor performance of the pipeline, since the ground truth value is relatively small.
- There is a strong positive linear correlation between the estimation results and the ground truth for both RR and HR, with the squared PCC value of 0.97 and 0.96 respectively over 13700 measurement points.
- The majority of measurement points (approximately 96%) demonstrate accurate estimations and lie in the region of LoA, with a small absolute error of less than 0.12 Hz for both RR and HR.

- 5.3% and 2.4% CV values for RR and HR respectively show the measurement points are relatively close to the mean with a low variability, while the reproducibility between estimation results and the ground truth is high, as evidenced by RPC values of 11% for RR and 4.7% for HR.

5

Measurement Setup and Experimental Data Acquisition

This chapter describes the radar parameters and procedures used in the experimental measurements for data acquisition. Besides, the approaches to obtain ground truth are also discussed. In Section 5.1, the radar information and the designed waveforms utilized to monitor the adult and the neonate, are introduced. Procedures for data collection and approaches to obtain ground truth for both adult data and neonate data are mentioned in Section 5.2, while a summary of the measurement setup and data acquisition is presented in Section 5.3.

5.1. Radar Parameters Selection

The experimental measurements for both adult and neonate are performed with the same radar. Throughout the data collection process, the radar is employed with specific waveforms tailored for different targets (adult or neonate), which are designed to optimize the radar's performance and capture the required vital signs accurately. Since the dataset of neonate is collected by C. Ramsey, the waveform used for neonate data collection is designed by C. Ramsey, so the waveform design process is discussed by using the adult data collection as an example.

5.1.1. Radar Information

To perform the data collection, the MIMO FMCW radar utilized in this thesis is the Texas Instruments IWR6843ISK mm-wave radar, the red board shown in Figure 5.1, operating at a carrier frequency f_c of 60 GHz. With high frequency, it allows for precise measurements and accurate detection of minute movements, making it ideal for monitoring vital signs for both adult and neonate. To get the raw ADC data for signal processing, there is a supporting board attached to the radar, the DCA1000EVM, which is the green board shown in Figure 5.1. Besides, the Millimeter Wave Studio graphical user interface (GUI) is used to extract the raw ADC data in a .bin file.

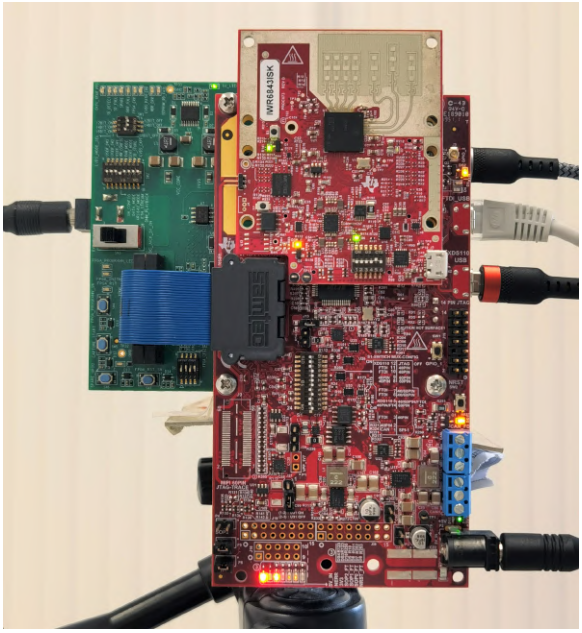

Figure 5.1: Texas Instruments IWR6843 mmWave radar used in this thesis, with the supporting board DCA1000EVM

5.1.2. WAVEFORM DESIGN

As previously mentioned in Table 2.1, the amplitude of the respiration and heartbeat has a small magnitude. Therefore, the relative motion of the chest is monitored rather than its exact position over time, which means the Doppler resolution is an important parameter and is required to capture the maximal velocities of the weakest respiration and heartbeat. With Eq. 2.1 and Eq. 2.4, the movement of the chest due to respiration and heartbeat is modeled, so the maximal velocities of the weakest respiration and heartbeat, which are the corresponding minimum Doppler resolutions Δv_{min}, can be expressed respectively as:

$$\begin{aligned} \Delta v_{min,r} &= max\left\{\frac{dR_r(t)}{dt}\right\}, \\ \Delta v_{min,h} &= max\left\{\frac{dR_h(t)}{dt}\right\}. \end{aligned} \tag{5.1}$$

After taking the derivative over time and applying the chain's rule, Eq. 5.1 becomes:

$$\begin{aligned} \Delta v_{min,r} &= max\left(a_{r,min} \cdot \pi f_{r,min} \cdot sin(2\pi f_{r,min} \cdot t)\right), \\ \Delta v_{min,h} &= max\left(-a_{h,min} \cdot 2\pi f_{h,min} \cdot sin(2\pi f_{h,min} \cdot t)\right). \end{aligned} \tag{5.2}$$

As the sine function can equal to 1 or -1, and a_{min} and f_{min} are time independent variables, this expression can be simplified to:

$$\begin{aligned} \Delta v_{min,r} &= a_{r,min} \cdot \pi f_{r,min}, \\ \Delta v_{min,h} &= a_{h,min} \cdot 2\pi f_{h,min}. \end{aligned} \tag{5.3}$$

After substituting a_{min} and f_{min} from Table 2.1 into Eq. 5.3, the maximal velocities for the weakest respiration and heartbeat are calculated to be around 0.0019 m/s simultaneously. Consequently, the minimum Doppler resolution Δv_{min} is supposed at least 0.0019 m/s to be able to track the weakest respiration and heartbeat of the adult. Doppler resolution primarily depends on the duration of the transmit frame expressed as:

$$T_{frame} = \frac{\lambda}{2 \cdot \Delta v}, \tag{5.4}$$

with λ is the wavelength. An increased number of chirps in a frame leads to improved Doppler resolution [70]. In other words, the longer the frame period, the better the Doppler resolution. Therefore, the minimum frame period must be at least 1.31 seconds.

Based on the requirements for Doppler resolution and the minimum frame period, the waveform is designed to collect the adult dataset. As for the frame period, it depends on the number of chirps transmitted within one frame and the chirp time, which can be calculated as:

$$T_{frame} = N_{chirp} \cdot T_{chirp}, \tag{5.5}$$

where N_{chirp} is the number of the chirps in each frame, T_{chirp} is the chirp time. Figure 5.2 depicts the frame structure, which contains several sequential chirps, and a single chirp with the main associated parameters for the waveform design.

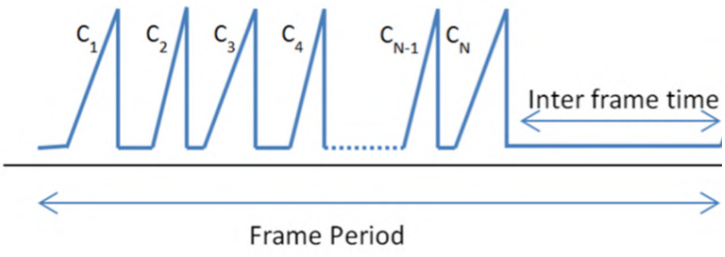

(a)

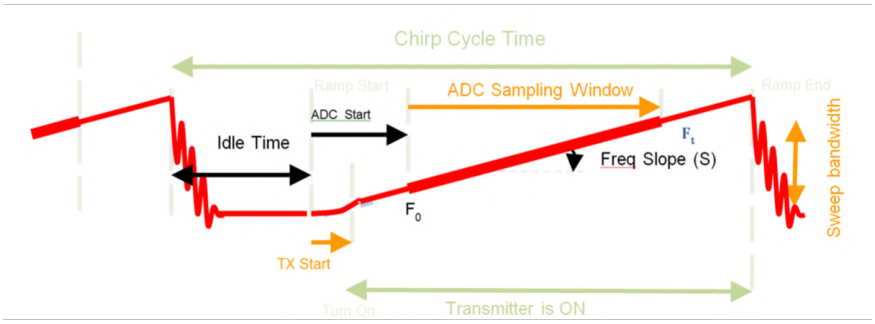

(b)

Figure 5.2: Frame structure and single chirp with related parameters [70]: (a) frame structure; (b) chirp structure with related parameters, where x axis shows the chirp period that consists of idle time and ramp time, y axis shows the bandwidth

As for a single chirp, the duration is given by:

$$T_{chirp} = T_{idle} + T_{ramp}, \tag{5.6}$$

where the idle time T_{idle} refers to the duration that the radar is not transmitting any signals, while the ramp time T_{ramp} is the effective time the transmitter is ON to send a single chirp. Besides, the ramp time is a significant parameter that decides the bandwidth B, which is the parameter refers to the range of frequencies used in the modulation of the transmitted continuous wave, with the equation as:

$$B = S \cdot T_{ramp}, \tag{5.7}$$

where S refers to the frequency slope as shown in Figure 5.2(b), describing the rate at which the frequency of the transmitted signal changes over time during the chirp period. Therefore, the ramp time also plays a key role in the definition of the range resolution ΔR, which can be expressed as:

$$\Delta R = \frac{c}{2 \cdot B}, \tag{5.8}$$

meaning that any increase of ramp time will lead to a finer range resolution. Since the maximum unambiguous range R_{max} can be determined by:

$$R_{max} = N_{adc} \cdot \Delta R, \tag{5.9}$$

where N_{adc} is the number of ADC samples per chirp, so the increasing of ramp time will result in the decrease of the maximum unambiguous range. The range resolution and maximum unambiguous range for the designed waveform are set as 5 cm and 6.4 m respectively, which is sufficient to track the adult in the proposed experiment scenario described in the next section.

Moreover, as the maximum unambiguous velocity V_{max} can be calculated as:

$$V_{max} = \frac{\lambda}{4 \cdot T_{chirp}}, \tag{5.10}$$

the ramp time plays an important role as well in the definition of the maximum unambiguous velocity. Besides, the number of chirps N_{chirp} and the idle time T_{idle} have a major impact on maximum unambiguous velocity and the velocity resolution according to Eq. 5.4, 5.5 and 5.10.

The key parameters of the two waveforms are summarized in Table 5.1. The waveform one is designed for adult data collection, which mainly focuses on having a proper velocity resolution to monitor the relative motion of the chest rather than the exact position to estimate the vital signs. Therefore, the total chirp period is designed to make it as long as possible by maximizing the number of the chirps in each frame and increasing the idle time, to achieve the required velocity resolution. As for the waveform two, it is used for neonate data collection designed by C. Ramsey, and the parameters are also listed in the following Table.

Parameter	W1 - Adult	W2 - Neonate
Carrier Frequency [GHz]	60	60
Frequency Slope [MHz/us]	30	65
Number of ADC samples per chip	128	200
Ramp Time [us]	100	51
Idle Time [us]	5160	13
Chip Duration [us]	5260	64
Number of chirps per frame	255	2
Frame Duration [ms]	1341	50
Bandwidth [MHz]	3000	3315
Range Resolution [cm]	5	4.5
Max. Unambiguous Range [m]	6.4	9
Velocity Resolution [m/s]	0.0019	0.05
Max. Unambiguous Velocity [m/s]	0.2376	19.53

Table 5.1: Summary of the key parameters of the two waveforms

5.2. DATA COLLECTION

As mentioned earlier, the data collection is divided into two parts: one part involves adult data collection and the other part involves neonate data collection, which is done by C. Ramsey. The measurement setup, measurement cases, and ground truth devices will be explained in this section.

5.2.1. ADULT DATA COLLECTION

For the adult data collection, the measurement setup in the indoor environment is shown in Figure 5.3. The target is sitting and positioned in front of the radar, with a distance varying from 0.3 m to 0.7 m between its chest and the radar. Then, the target is required to perform the measurement cases to execute the data with ground truth devices attached to the body. During the measurement, two different cases are performed to collect data, while the target is required to carry out different behavior, including breathing normally, breathing fast, holding breath, and RBM. And the measurement cases are summarized as:

- Measurement case 1
  - Scenario: Sitting + Breath normally
  - Waveform: W1 - Adult
  - Distance: Vary from 0.3 m to 0.7 m
  - Test duration: 80 s
    - Sitting + Breath normally 0 - 20 s
    - RBM 20 - 30 s
    - Sitting + Breath normally 30 - 50 s
    - RBM 50 - 60 s

- Sitting + Breath normally 60 - 80 s

- Measurement case 2
  - Scenario: Sitting + Breath normally + Breath fast + Hold breath
  - Waveform: W1 - Adult
  - Distance: Vary from 0.3 m to 0.7 m
  - Test duration: 210 s
    - Sitting + Breath normally 0 - 50 s
    - RBM 50 - 60 s
    - Sitting + Breath fast 60 - 110 s
    - RBM 110 - 120 s
    - Sitting + Breath normally 120 - 170 s
    - Sitting + Hold breath 170 - 190 s
    - Sitting + Breath normally 190 - 210 s

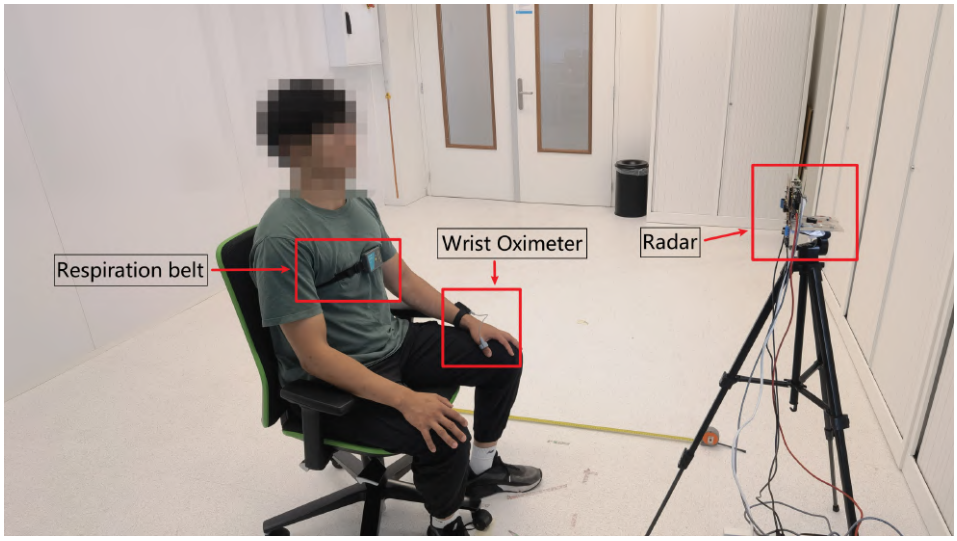

Figure 5.3: Measurement setup for adult data collection

Additionally, in the adult data collection, data from 6 different measurement targets are acquired, with 3 females and 3 males. Table 5.2 shows the information of the measurement targets, including the gender, age, height, weight, body mass index (BMI), clothes worn by each of the targets during the data collection, also the measurement case for each target.

Gender	Age	Height [cm]	Weight [kg]	BMI	Clothes	Measurement case
1. Male	24	170	67	23.2	T-shirt	Case 1
2. Female	24	165	54	19.8	T-shirt	Case 1, 2
3. Male	25	183	82	24.5	T-shirt	Case 1, 2
4. Female	22	166	61	22.1	Sweatshirt	Case 2
5. Female	23	158	65	25.4	Blouse	Case 2
6. Male	26	180	81	25.0	T-shirt	Case 2

Table 5.2: Summary of the information and the measurement case for each each measured adult target

As for the ground truth device, the Go Direct respiration belt, as shown in Figure 5.4(a), is utilized to measure the force exerted on the chest during breathing. With the same STFT algorithm applied to the force data, the ground truth of RR can be obtained. As shown in Figure 5.4(b), the Checkme O2 Max wrist oximeter is worn on the wrist, which will return an HR value every 2 seconds with a resolution of 1 bpm as ground truth.

(a)

(b)

Figure 5.4: Ground truth device: (a) Go Direct respiration belt [71]; (b) Checkme O2 Max Wrist Oximeter [72]

5.2.2. NEONATE DATA COLLECTION

For the neonate data collection, the radar and its supporting board are placed in a container that will be sanitized after measurement, as shown in Figure 5.5. The outside of the container is made of plastic, so the radar signal can still pass through the box and measure the chest movement of the neonate. The addition of plastic between the radar and the neonate adds more distortion to the signal. Considering it can prevent the radar from being shocked by hanging stably above the incubator or crib and also allow for the sanitation of the entire container after measurement, the container is still utilized.

During the measurement, the neonate is placed in the open bed crib and covered by clothing and blankets, as shown in Figure 5.6. The open bed crib does not have a plastic casing above the neonate as the incubator, which means the signal is less distorted. Besides, there is a steel arm hanging the radar above the neonate with a distance of 0.5 meters, and the radar can be identified by the small lights in Figure 5.6, indicating that measurement is in progress. As for the ground truth device, the conventional medical ECG machine with contact sensors, which can also be seen in Figure 5.6, is used for the neonate at the same time to record RR and HR in bpm each second, having a resolution of 1 bpm.

Figure 5.5: Supporting board with the radar in the plastic container, used for the data collection on neonates performed by C. Ramsey at Erasmus Medical Center [8]

Figure 5.6: Radar taking measurements of neonate in open bed [8]

5.3. SUMMARY

This chapter firstly introduces the radar which is utilized in the experimental measurements, and also describes the interrelation between various radar parameters by listing equations and analysing the impact of the parameters. Afterwards, the radar waveform used in adult data collection is designed based on the requirements of Doppler resolution and frame period, which mainly focuses on having a proper velocity resolution to monitor the relative motion of the chest rather than the exact position to estimate the vital signs. Besides, the waveform used for neonate data collection, which is designed by C. Ramsey in her work in [8], is also listed in Table 5.1. Next, the measurement setup and scenarios for both adult and neonate data collection are presented, providing detailed descriptions and accompanying figures. As for ground truth devices, a respiration belt and a wrist oximeter are used in the measurement of adults, while the conventional medical ECG machine is employed for the neonate measurement.

6

EXPERIMENTAL VALIDATION AND RESULT ANALYSIS

The validation of the proposed processing pipeline for RR and HR estimation is described in this chapter, based on analysing the result of the experimental data collected as described in the previous chapter. Section 6.1 and Section 6.2 discuss the experiment result analysis for adult data and neonate data respectively. Section 6.3 investigates whether the data from different channels of the MIMO FMCW radar will have an influence on the estimation performance. In the end, a summary of the performance of the proposed processing pipeline in vital signs monitoring is shown in Section 6.4.

6.1. ADULT EXPERIMENT RESULT ANALYSIS

For the adult data, it is measured under two different measurement cases, and the data of both cases is utilized to evaluate the selection of data segments and range bins, while only the data of case 2 is used to evaluate the estimation of vital signs.

6.1.1. DATA SEGMENT AND RANGE BIN

In measurement case 1, the RBM occurs in two periods: from 20 to 30 seconds and from 50 to 60 seconds. While the RBM takes place from 50 to 60 seconds and from 110 to 120 seconds in measurement case 2. Consequently, a total of 24 data segments are expected to be selected. The results of the data segment and range bin selection for each target are presented in Table 6.1, with the font of incorrect selections highlighted in bold.

The data segment selection process resulted in the identification of 25 data segments. However, there is an issue with the third segment of target 6, which is divided into two pieces, and the 20 seconds of data in the middle is incorrectly identified as having RBM. Additionally, two other segments are mistakenly determined with 10 seconds less time. As a result of these inaccuracies, there are 4 segments selected incorrectly out of the 25 segments, which means an accuracy rate at 87.5%.

Regarding the range bin selection, the ground truth is determined through manual

selection based on the range-time map. After comparison, it is found that only two range bins are selected incorrectly. However, the differences from the ground truth for both cases are only 0.05 meters, indicating that the selected range bins are adjacent to the actual ground truth range bins. Overall, there are 2 segments with incorrect range bin selection out of the 25 segments, leading to a 92.0% accuracy rate for the range bin selection. Therefore, the proposed processing pipeline is proved to be satisfactory for the selection of data segment and range bin in the case of adult data, with in total 6 data segments having mistakes, 4 for data segment selection and 2 for range bin selection, as shown in Table 6.1 with bold font.

Target	**Case**	**Segment [s]**	**Estimated range bin [m]**	**Ground truth [m]**
1. Male	1	0 - 20	0.50	0.50
		30 - 50	0.50	0.50
		60 - 80	**0.45**	**0.50**
2. Female	1	0 - 20	0.45	0.45
		30 - 50	0.45	0.45
		60 - 80	**0.45**	**0.40**
	2	**0 - 40**	0.35	0.35
		60 - 110	0.35	0.35
		120 - 210	0.35	0.35
3. Male	1	0 - 20	0.50	0.50
		30 - 50	0.45	0.45
		60 - 80	0.50	0.50
	2	0 - 50	0.35	0.35
		60 - 110	0.35	0.35
		120 - 210	0.35	0.35
4. Female	2	**10 - 50**	0.35	0.35
		60 - 110	0.35	0.35
		120 - 210	0.35	0.35
5. Female	2	0 - 50	0.50	0.50
		60 - 110	0.50	0.50
		120 - 210	0.50	0.50
6. Male	2	0 - 50	0.45	0.45
		60 - 110	0.50	0.50
		120 - 150	0.50	0.50
		170 - 210	0.50	0.50

Table 6.1: Data segment and range bin selection results of adult data, where the incorrect selections in terms of either data segment detection or range bin are highlighted by the bold font

6.1.2. RESPIRATION AND HEARTBEAT ESTIMATION RESULT

After processing the data with the proposed STFT algorithm, the estimation results are generated, based on which, the properties of the absolute error and the relative error can be calculated and presented in Table 6.2.

For RR estimation, under the absolute error scenario, the maximum error is 0.268 Hz, indicating the deviation from the ground truth is at a low level compared to the simulation results. Conversely, the maximum relevant error is 137.6%, which is because of the relatively small ground truth. Additionally, the minimum error is 0 Hz for both cases, suggesting that there are measurement points where the estimation aligns perfectly with the ground truth. With an average error of 0.044 Hz or 14.4%, the overall bias of the estimation is at a promising level. The standard deviation of 0.088 Hz or 16.1% highlights the errors are more dispersed compared to the simulation results, since the individual differences in RR frequency between the targets can be more prominent.

Regarding HR estimation, the maximum error is 0.706 Hz and the average error is 0.117 Hz, under the absolute error condition, which is much larger than the error of RR. The reason can be the amplitude of the heartbeat is smaller than respiration, making it more challenging for the radar to capture accurately. And comparing to simulation results, the mean of the error has a noticeable increase, also confirming the viewpoint that HR is more challenging to estimate. Even so, the minimum error is still at 0 Hz, implying perfect matches between the estimation results and ground truth can still exist. Due to the same reason, the standard deviation values are larger than the simulation results, but still remain at a decent level.

Property of error	**Type of error**	**Respiration rate**	**Heartbeat rate**
Maximum	Absolute [Hz]	0.268	0.706
	Relative [%]	137.6	55.9
Minimum	Absolute [Hz]	0	0
	Relative [%]	0	0
Mean	Absolute [Hz]	0.044	0.117
	Relative [%]	14.4	7.7
Standard deviation	Absolute [Hz]	0.088	0.105
	Relative [%]	16.1	6.4

Table 6.2: Error properties of adult data results, where five different adult targets measured in experiment case 2 are evaluated

With results of approximately 1300 measurement points, the correlation graph and Bland-Altman plot are drawn as presented in Figure 6.1, 6.2. The values of the squared PCC stand at 0.92 and 0.73 for RR and HR respectively, indicating the positive linear correlation between the estimation results and the ground truth is stronger in RR, which also can be observed in the correlation graph. For RR estimation, the data points are divided into two groups and the group with higher frequency has roughly three times as many points as the group with lower frequency. This confirms the fact that in case 2, the time spent in normally breathing is roughly three times longer than fast breathing. For HR estimation, the data points are also divided into two groups, due to the fact that target 3 and 4 have a relatively high HR compared to other targets, as shown in Table 6.3.

According to the Bland-Altman plot, 19% and 10% CV values for RR and HR respectively demonstrate the measurement points have a low variability, with only a small proportion deviating significantly from the mean value. With 26% and 20% of RPC values for RR and HR, the reproducibility and agreement are lower between estimation results and

the ground truth compared to the simulation results, which also indicates that there are relatively moderate fluctuations in estimation results. Overall, while the result of adult monitoring is not as good as the simulation results, but it still demonstrates an adequate performance, which can validate the proposed processing pipeline.

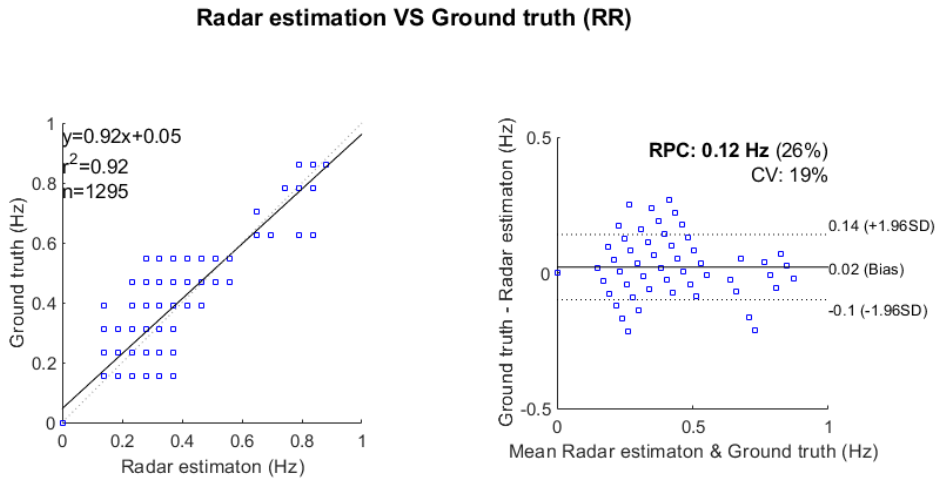

Figure 6.1: Correlation graph and Bland-Altman plot of RR estimation, showing the relation between the estimation results and ground truth (adult data)

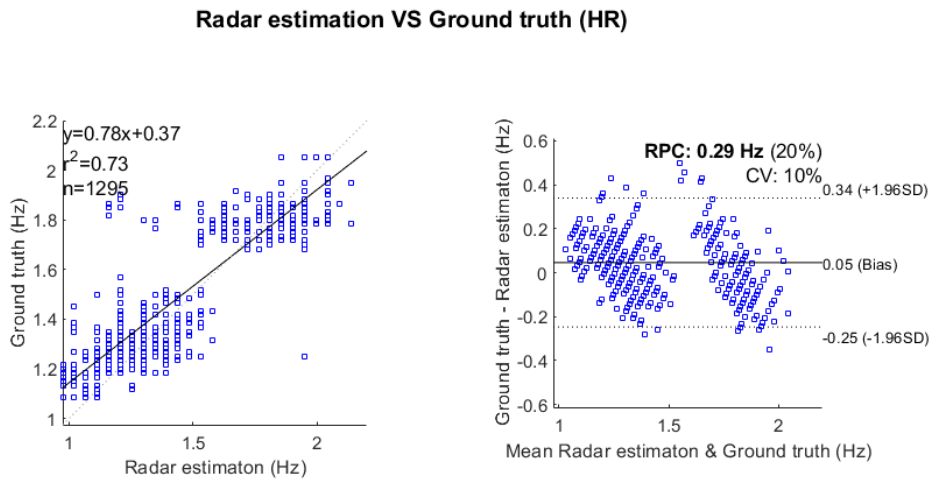

Figure 6.2: Correlation graph and Bland-Altman plot of HR estimation, showing the relation between the estimation results and ground truth (adult data)

Average ground truth value	Target 1	Target 2	Target 3	Target 4	Target 5
Respiration [Hz]	0.223	0.293	0.253	0.471	0.406
Heartbeat [Hz]	1.257	1.292	1.763	1.801	1.316

Table 6.3: Average ground truth value for each adult target

The individual analysis is provided by the bar graphs in Figure 6.3, which show the absolute error properties of estimation results for each adult target. With the minimum errors staying at zero, it is clear that there exists accurate estimation for each target in both RR and HR estimation. For each individual target, the variation in maximum error is relatively pronounced, which may be due to individual differences and experimental errors, while the mean and standard deviation of the error maintain relative stability. For target 3, the maximum error for both RR and HR is relatively larger compared to other targets. The reason can be that target 3 wore a relatively loose sweatshirt, making it more challenging for the radar to capture vital sign signals.

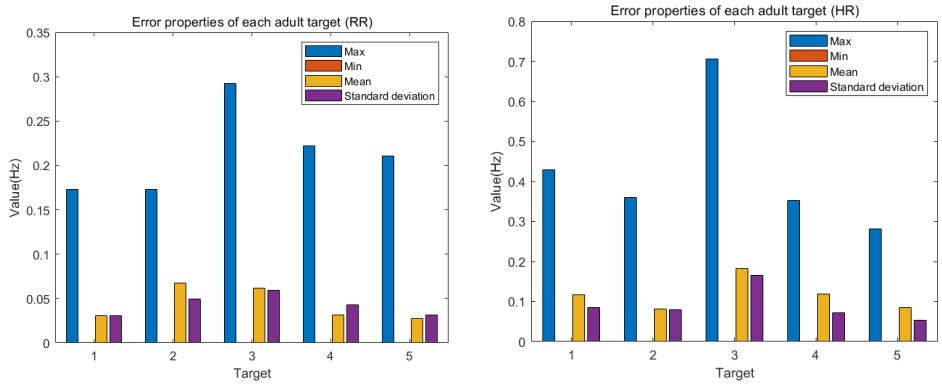

(a) (b)

Figure 6.3: Absolute error properties of estimation results for each adult target, note that the scale of the Y axis is different for RR (left) and HR (right) results: (a) Absolute error properties of RR estimation results; (b) Absolute error properties of HR estimation results

6.2. NEONATE EXPERIMENT RESULT ANALYSIS

The neonate data is measured by C. Ramsey as described in the previous chapter, and the data are gathered from 6 different neonates. All the data will be utilized to evaluate the selection of data segments and range bins as well as the performance of vital signals estimation.

6.2.1. DATA SEGMENT AND RANGE BIN

As the neonate data is collected by others, the occurrence of body movement is not explicitly recorded, so there is no ground truth for data segment selection, meaning that it

is not possible to make a precise assessment. However, by utilizing the information in the range-time map, it is possible to demonstrate that the proposed processing pipeline can detect a significant portion of the occurrence of body movement, based on which, 20 data segments are selected for the further process, as presented in Table 6.4.

As for the range bin selection, the ground truth is determined through manual selection based on the range-time map. According to Table 6.4, it is found that only two range bins are selected incorrectly, which are highlighted by the bold font. However, the differences from the ground truth for both cases are only 0.04 meters, indicating that the selected range bins are adjacent to the actual ground truth range bins. Hence, out of the 20 segments, there are 2 segments with incorrect range bin selections, resulting in an overall accuracy rate of 90.0% for the range bin selection. Additionally, it is evident that neonate monitoring involves longer-term observation, so the range bin will continuously change over time because of the movement of the neonate. Therefore, regarding the neonate data, the proposed processing pipeline is also proved to be satisfactory for the dynamic range bin selection.

Target	**Segment [s]**	**Estimated range bin [m]**	**Ground truth [m]**
1	20 - 60	0.46	0.46
	180 - 240	0.46	0.46
	300 - 360	0.46	0.46
2	250 - 450	0.46	0.46
	650 - 750	**0.5**	**0.46**
	1000 - 1150	0.5	0.5
3	1900 - 2000	0.42	0.42
	2300 - 2450	0.42	0.42
4	400 - 800	0.5	0.5
	1000 - 1800	0.5	0.5
5	1 - 60	0.5	0.5
	80 - 140	0.46	0.46
	200 - 320	**0.46**	**0.5**
6	350 - 550	0.5	0.5
	850 - 950	0.54	0.54
	1100 - 1200	0.5	0.5
	2150 - 2250	0.5	0.5
	2350 - 2450	0.54	0.54
	2700 - 2800	0.54	0.54
	2850 - 2950	0.5	0.5

Table 6.4: Data segment and range bin selection results of neonate data, where the incorrect selections are highlighted by the bold font

6.2.2. RESPIRATION AND HEARTBEAT ESTIMATION RESULT

With the proposed STFT algorithm, estimation results can be generated and the properties of the absolute error and the relative error can be calculated and listed as shown in Table 6.5. Focusing on RR estimation, the maximum absolute error of 0.535 Hz is larger than the corresponding value of adult results, while being smaller than simulation results. This is due to the increased complexity in neonate monitoring compared to adult monitoring, while more extreme circumstances may occur in the simulation scenario such as intense fluctuations in both RR and HR. On the other hand, all the properties in relative error are smaller than the results of adult data. It is because the neonates have a faster RR value than the adults, which means a higher ground truth, which will lead to a lower relative error. Besides, the minimum values for both types of error are 0, which points to instances where the algorithm precisely estimates the RR. Last but not least, the mean and standard deviation for both types of error are at a low level, demonstrating that the majority of measurement points have small errors and relatively low variability.

In terms of HR estimation, with the same reason as RR estimation, a similar phenomenon is observed in the maximum absolute error. Furthermore, the HR values of the neonate are even higher, with some reaching up to 3 Hz, so the maximum relative error is decreasing while the maximum absolute error is at the same level as adult results. Conversely, the mean and standard deviation are increasing compared to the adult results, under the absolute error scenario, which proves the increased complexity in neonate monitoring again. Additionally, the mean of absolute error is even three times larger for HR estimation, comparing to the RR estimation, while it is also higher than the corresponding value of adult results, indicating the estimation for HR of neonate faces more challenges, with a smaller size of the heart.

Property of error	Type of error	Respiration rate	Heartbeat rate
Maximum	Absolute [Hz]	0.535	0.724
	Relative [%]	62.4	36.1
Minimum	Absolute [Hz]	0	0
	Relative [%]	0	0
Mean	Absolute [Hz]	0.056	0.143
	Relative [%]	6.7	5.9
Standard deviation	Absolute [Hz]	0.061	0.123
	Relative [%]	7.4	5.1

Table 6.5: Error properties of neonate data results, where six different neonates are evaluated

With the estimation encompassing approximately 5000 measurement points, the correlation graph and Bland-Altman plot are illustrated in Figure 6.4, 6.5. As shown in the correlation graph, the values of the squared PCC are 0.81 and 0.55 for RR and HR respectively, means that RR has a stronger positive linear correlation between the estimation results and the ground truth, while the positive linear correlation of HR is weaker.

Based on the Bland-Altman plot, compared to the adult results, the measurement points have a lower variability, that means only a minority display significant deviations from the mean value, which is evidenced by the 9.4% and 7.3% CV values for RR and HR

respectively. With 0.16 Hz and 0.35 Hz of RPC values for RR and HR, the reproducibility and agreement are lower between estimation results and the ground truth compared to the adult results, while RPC values in percentage are decreasing because of the increasing of the ground truth values as shown in Table 6.6. And it also indicates that there are relatively larger fluctuations in estimation results. Overall, as expected, the result of neonate monitoring falls short of the performance achieved in adult results, due to the increased complexity in neonate monitoring. However, it still showcases a sufficient level of performance, which serves to validate the proposed processing pipeline.

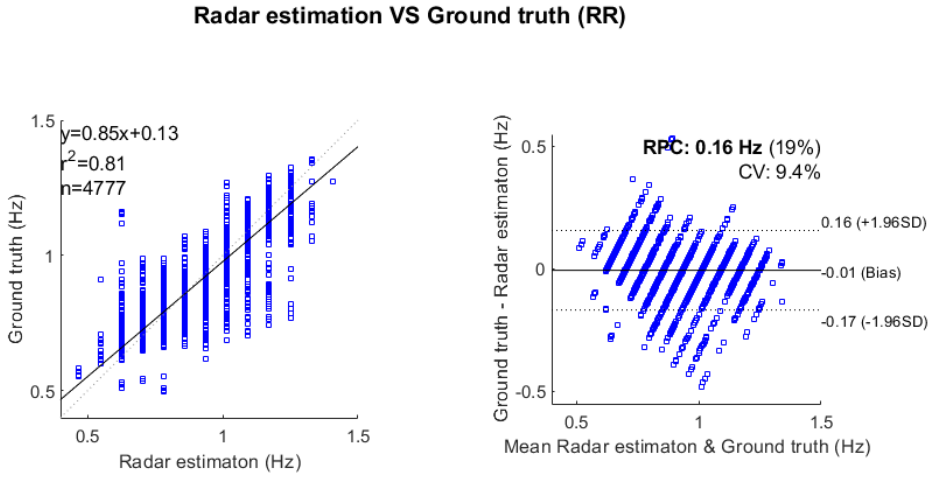

Figure 6.4: Correlation graph and Bland-Altman plot of RR estimation, showing the relation between the estimation results and ground truth (neonate data)

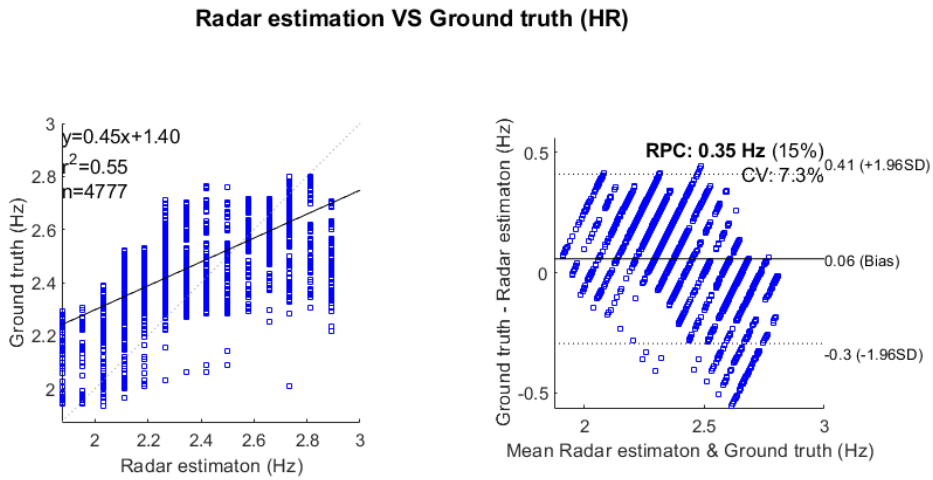

Figure 6.5: Correlation graph and Bland-Altman plot of HR estimation, showing the relation between the estimation results and ground truth (neonate data)

Average ground truth value	Target 1	Target 2	Target 3	Target 4	Target 5	Target 6
Respiration [Hz]	0.827	0.896	0.786	0.756	0.963	1.082
Heartbeat [Hz]	2.457	2.411	2.373	2.638	2.549	2.336

Table 6.6: Average ground truth value for each neonate target

The individual analysis is provided by the bar graphs in Figure 6.6, which show the absolute error properties of estimation results for each neonate target. Unlike the adult results, the minimum errors of HR for target 1 and target 2 are not zero. Once again, it proves the increased complexity in neonate monitoring. Compared to adults, there is a larger individual difference in the RR and HR in neonates, which can be evidenced by Table 6.6 showing the average ground truth values and the variation of the mean errors, particularly noticeable in the case of HR. Besides, the errors in HR are generally significantly larger than those in RR, which also proves a smaller size of the heart makes it more challenging for the radar to capture vital sign signals.

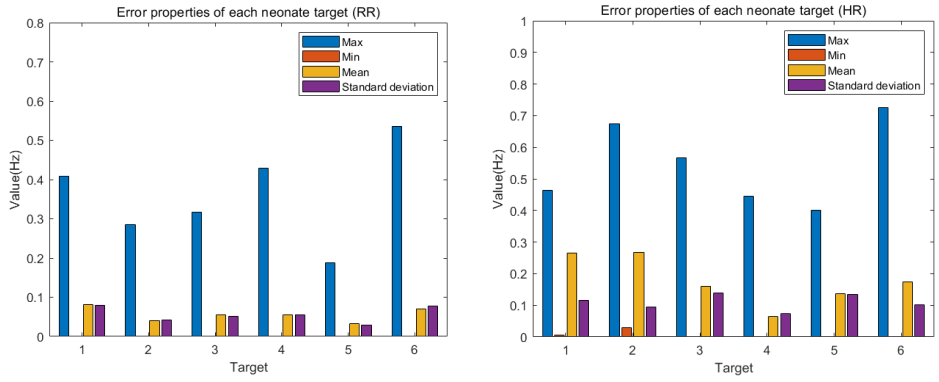

(a) (b)

Figure 6.6: Absolute error properties of estimation results for each neonate target, note that the scale of the Y axis is different for RR (left) and HR (right) results: (a) Absolute error properties of RR estimation results; (b) Absolute error properties of HR estimation results

6.3. CHANNEL INVESTIGATION

Since the MIMO FMCW radar is utilized in this thesis project, an investigation is conducted to examine the potential impact of data from different MIMO radar channels on vital signs monitoring. The core focus of the investigation involves processing the data from different radar channels individually, and conducting a comparative analysis of the results. To facilitate this investigation, a total of eight data segments are chosen for processing, half are adult data and the other half are neonate data.

For each data segment, four sets of data derived from the individual receiver of the radar, along with the sum and the mean of those four sets of data, form a new dataset. Subsequently, the mean absolute error is calculated for each estimation result, and the

channel with the lowest mean absolute error is identified as the best performance channel and listed in the following Table 6.7, where Seg k represents the number of the analysed data segment, C1-C4 represents the channel 1-4, C5 represents the sum of those four channels of data, C6 represents the mean of those four channels of data. It is clear that neither RR nor HR has a channel that always leads to the lowest mean absolute error, indicating that the performance of the channel's data varies, so there is not a single channel that consistently outperforms others, at least with the collected data.

Best performance channel	**Seg 1**	**Seg 2**	**Seg 3**	**Seg 4**	**Seg 5**	**Seg 6**	**Seg 7**	**Seg 8**
Respiration	C5	C3	C5	C2	C4	C6	C2	C3
Heartbeat	C6	C2	C4	C3	C1	C2	C2	C4

Table 6.7: Best performance channel for each segment in RR and HR, based on which channel has the lowest mean absolute error, where Seg k represents the number of the analysed data segment, C1-C4 represents the channel 1-4, C5 represents the sum of those four channels of data, C6 represents the mean of those four channels of data

6.4. SUMMARY

In this chapter, the validation of the proposed processing pipeline is conducted through processing of experimental data for both adults and neonates. To have a comprehensive evaluation of the performance of the proposed processing pipeline, tables about the results of the data segment and range bin selection with their corresponding ground truth are listed, while tables about properties of error, correlation graphs, Bland-Altman plots, and bar graphs for individual target analysis are generated based on the RR and HR estimation results, showing:

- With an 87.5% accuracy for adult data segment selection, the proposed method demonstrates its successful functionality. As for the neonate data, where ground truth is unavailable, it is still possible to demonstrate that the proposed method can detect a significant portion of the occurrence of body movement, based on the information of the range-time map. Regarding range bin selection, the accuracies are 92% and 90% respectively for adult case and neonate case, indicating satisfactory outcomes.
- For adult data, the minimum errors are zero, which means accurate measurements are still attainable in real measurement data. The mean and the standard deviation increase noticeably compared to the simulation results, while a lower maximum error occurs, since there is no rapid fluctuations of RR in real case. Compared to simulation results, the positive linear correlation between the estimation results and the ground truth is weaker, while the increases of RPC and CV values mean less reproducibility and agreement and larger variability.
- For neonate data, the minimum of the errors remains at zero, meaning that accurate measurements are still attainable in more complicated situations. While the mean and the standard deviation keep increasing compared to the adult results,

due to the increased complexity in neonate monitoring. Maximum relative errors decrease obviously, primarily because of the higher ground truth values. Besides, the positive linear correlation keeps weakening. The CV values decrease with a lower variability of the estimation results, while the reproducibility and agreement keep decreasing evidenced by absolute RPC values.

- By processing the real data segments, it is shown that the result of each MIMO channel's data varies, so there is not a single channel that consistently outperforms others, at least with the collected data.

7

CONCLUSION AND RECOMMENDATION

As a closure, Section 7.1 summarizes the key results of the thesis. Finally, a few recommendations for the work of this thesis are shared in Section 7.2, mentioning several future directions of work to pursue.

7.1. CONCLUSION

The main results of this thesis project can be summarized as follows:

- The proposed methods for automatically identifying the ideal data segment, where there is no body movement occurring, and selecting the optimal range bin, which is most relevant to the vital sign signals, have demonstrated effective performance in both adult and neonate processing, achieving an accuracy of 90% approximately.
- The Doppler resolution plays a critical role in enabling the radar to monitor vital signs successfully. In the designed waveform 1, a Doppler resolution of 0.0019 m/s is achieved to capture the maximal velocities of the weakest respiration or heartbeat. A finer Doppler resolution enhances the ability of the radar to detect the weakest vital sign signals, resulting in improved performance in estimating RR and HR.
- Compared to the simulation results, the experimental results exhibit smaller maximum values of absolute error, proving that the waveform with three random inputs designed in the Monte Carlo test is critical enough to simulate RR and HR of the neonate effectively, and some of their abrupt changes may not even occur in real life scenario.
- For the estimation results, a larger relative error does not necessarily indicate a poor performance of the pipeline, as it may be influenced by the relatively small

ground truth value, especially for the case where there are only a few measurement points with significant deviations.

- From the simulation data to real adult data, and further to neonate data, the measurement errors are gradually increasing, and it can be seen from the increasing of the mean errors, which is increasing from 0.029 Hz to 0.117 Hz to 0.143 Hz in the case of HR. Even so, the majority of measurement errors remain within an acceptable range, which proves the performance of the pipeline. Besides, the result of each channel's data varies, so there is not a single channel that consistently outperforms others.

7.2. RECOMMENDATION

Based on the results of this thesis project, some recommendations are drawn as follows:

- Verify the effectiveness of the pipeline for vital signs monitoring at longer distances from the radar and under unfavorable aspect angles. Comprehensively assess the robustness and suitability of the proposed processing pipeline for vital signs monitoring in those conditions.
- Expand the current capabilities to encompass the successful monitoring of other vital signs, such as blood oxygen and blood pressure. Conduct new measurements for neonates to record the ground truth of all the vital signs, as well as the occurrence of the body movement.
- Based on the intensity of the motion, categorize body movement into different levels. Process the data segments that contain body movement and assess the influence of different level body movements on the RR and HR estimation results. Consider employing other signal processing techniques to mitigate the effects of body movement.
- Evaluate the impact of different layers of clothing worn by the monitored people on the RR and HR estimation results. Assess how different orientations in relation to the radar, such as side, rear, and top views, affect the estimation results of RR and HR.
- Explore the feasibility of using the existing radar system to estimate RR and HR for multiple people simultaneously, and the inspiration can be drawn from the work of Dirk in [73].
- Investigate modifications to the radar system, such as hybridizing with a camera system, to achieve better estimation performance or more advanced capability.

BIBLIOGRAPHY

[1] World Health Organization, *Born too soon: The global action report on preterm birth*, 2012.

[2] J. Zhao, F. Gonzalez, and D. Mu, "Apnea of prematurity: From cause to treatment," *European journal of pediatrics*, vol. 170, pp. 1097–1105, 2011.

[3] G. Beltrão, R. Stutz, F. Hornberger, *et al.*, "Contactless radar-based breathing monitoring of premature infants in the neonatal intensive care unit," *Scientific Reports*, vol. 12, no. 1, p. 5150, 2022.

[4] H. Verder, K. Bohlin, J. Kamper, R. Lindwall, and B. Jonsson, "Nasal cpap and surfactant for treatment of respiratory distress syndrome and prevention of bronchopulmonary dysplasia," *Acta paediatrica*, vol. 98, no. 9, pp. 1400–1408, 2009.

[5] J. Perin, A. Mulick, D. Yeung, *et al.*, "Global, regional, and national causes of under-5 mortality in 2000–19: An updated systematic analysis with implications for the sustainable development goals," *The Lancet Child & Adolescent Health*, vol. 6, no. 2, pp. 106–115, 2022.

[6] J. D. Kim, W. H. Lee, Y. Lee, *et al.*, "Non-contact respiration monitoring using impulse radio ultrawideband radar in neonates," *Royal Society open science*, vol. 6, no. 6, p. 190 149, 2019.

[7] J. M. Di Fiore, "Neonatal cardiorespiratory monitoring techniques," in *Seminars in neonatology*, Elsevier, vol. 9, 2004, pp. 195–203.

[8] C. Ramsey, L. Baker, and F. Fioranelli, "Contactless monitoring of neonates in the intensive care unit," in *Project Report*, Open Mind Call part of the Convergence Initiative between TU Delft, Erasmus MC, and Erasmus University, 2022.

[9] EvergreenHealth, *Neonatal intensive care unit (nicu)*, Last accessed 28 January 2023, 2023. [Online]. Available: https://www.evergreenhealth.com/health-services/pregnancy-birth/after-birth/nicu/.

[10] M. Villarroel, A. Guazzi, J. Jorge, *et al.*, "Continuous non-contact vital sign monitoring in neonatal intensive care unit," *Healthcare technology letters*, vol. 1, no. 3, pp. 87–91, 2014.

[11] A. K. Abbas, K. Heimann, K. Jergus, T. Orlikowsky, and S. Leonhardt, "Neonatal non-contact respiratory monitoring based on real-time infrared thermography," *Biomedical engineering online*, vol. 10, no. 1, pp. 1–17, 2011.

[12] L. Maurya, P. Kaur, D. Chawla, and P. Mahapatra, "Non-contact breathing rate monitoring in newborns: A review," *Computers in Biology and Medicine*, vol. 132, p. 104 321, 2021.

[13] Convergence, *Convergence framework*, Last accessed 12 August 2023, 2023. [Online]. Available: https://convergence.nl/nl/.

[14] A. Al-Naji and J. Chahl, "Detection of cardiopulmonary activity and related abnormal events using microsoft kinect sensor," *Sensors*, vol. 18, no. 3, p. 920, 2018.

[15] J. Tu, K. Inthavong, G. Ahmadi, J. Tu, K. Inthavong, and G. Ahmadi, "The human respiratory system," *Computational fluid and particle dynamics in the human respiratory system*, pp. 19–44, 2013.

[16] S. Humagain, *Mechanism of breathing and its neural regulation*, Last accessed 03 February 2023, 2022. [Online]. Available: https://onlinesciencenotes.com/mechanism-of-breathing-and-its-neural-regulation/.

[17] A. De Groote, M. Wantier, G. Chéron, M. Estenne, and M. Paiva, "Chest wall motion during tidal breathing," *Journal of Applied Physiology*, vol. 83, no. 5, pp. 1531–1537, 1997.

[18] S. Fleming, M. Thompson, R. Stevens, *et al.*, "Normal ranges of heart rate and respiratory rate in children from birth to 18 years of age: A systematic review of observational studies," *The Lancet*, vol. 377, no. 9770, pp. 1011–1018, 2011.

[19] G. Gouna, T. Rakza, E. Kuissi, T. Pennaforte, S. Mur, and L. Storme, "Positioning effects on lung function and breathing pattern in premature newborns," *The Journal of pediatrics*, vol. 162, no. 6, pp. 1133–1137, 2013.

[20] S. Reuter, C. Moser, and M. Baack, "Respiratory distress in the newborn," *Pediatrics in review*, vol. 35, no. 10, p. 417, 2014.

[21] A. B. te Pas, C. Wong, C. O. F. Kamlin, J. A. Dawson, C. J. Morley, and P. G. Davis, "Breathing patterns in preterm and term infants immediately after birth," *Pediatric research*, vol. 65, no. 3, pp. 352–356, 2009.

[22] G. Paterniani, D. Sgreccia, A. Davoli, *et al.*, "Radar-based monitoring of vital signs: A tutorial overview," *Proceedings of the IEEE*, 2023.

[23] M. Baldi, F. Appignani, B. Zanaj, and F. Chiaraluce, "Body movement compensation in uwb radars for respiration monitoring," in *2012 IEEE First AESS European Conference on Satellite Telecommunications (ESTEL)*, IEEE, 2012, pp. 1–6.

[24] F. Weishaupt, I. Walterscheid, O. Biallawons, and J. Klare, "Vital sign localization and measurement using an lfmcw mimo radar," in *2018 19th International Radar Symposium (IRS)*, IEEE, 2018, pp. 1–8.

[25] J. E. Hall and M. E. Hall, *Guyton and Hall textbook of medical physiology e-Book*. Elsevier Health Sciences, 2020.

[26] R. Bailey, *The cardiac cycle*, Last accessed 06 February 2023, 2020. [Online]. Available: https://www.thoughtco.com/phases-of-the-cardiac-cycle-anatomy-373240.

[27] G Ramachandran and M Singh, "Three-dimensional reconstruction of cardiac displacement patterns on the chest wall during the p, qrs and t-segments of the ecg by laser speckle inteferometry," *Medical and Biological Engineering and Computing*, vol. 27, pp. 525–530, 1989.

[28] S. Weinberge, *Arrhythmia (abnormal heartbeat)*, Last accessed 06 February 2023, 2022. [Online]. Available: https://kidshealth.org/en/parents/arrhythmias.html.

[29] D. R. Morgan and M. G. Zierdt, "Novel signal processing techniques for doppler radar cardiopulmonary sensing," *Signal Processing*, vol. 89, no. 1, pp. 45–66, 2009.

[30] E. Pittella, B. Zanaj, S. Pisa, and M. Cavagnaro, "Measurement of breath frequency by body-worn uwb radars: A comparison among different signal processing techniques," *IEEE Sensors Journal*, vol. 17, no. 6, pp. 1772–1780, 2017.

[31] S.-w. Kang, M.-h. Jang, and S. Lee, "Identification of human motion using radar sensor in an indoor environment," *Sensors*, vol. 21, no. 7, p. 2305, 2021.

[32] S. Venkatesh, C. R. Anderson, N. V. Rivera, and R. M. Buehrer, "Implementation and analysis of respiration-rate estimation using impulse-based uwb," in *MILCOM 2005-2005 IEEE Military Communications Conference*, IEEE, 2005, pp. 3314–3320.

[33] A. Nezirovic, A. G. Yarovoy, and L. P. Ligthart, "Signal processing for improved detection of trapped victims using uwb radar," *IEEE Transactions on Geoscience and Remote Sensing*, vol. 48, no. 4, pp. 2005–2014, 2009.

[34] A. Nezirovic, "Stationary clutter-and linear-trend suppression in impulse-radar-based respiratory motion detection," in *2011 IEEE International Conference on Ultra-Wideband (ICUWB)*, IEEE, 2011, pp. 331–335.

[35] Q. Qi, Y. Zhao, L. Zhang, Z. Yang, L. Sun, and X. Jia, "Research on ultra-wideband radar echo signal processing method based on p-order extraction and vmd," *Sensors*, vol. 22, no. 18, p. 6726, 2022.

[36] Y. Xu, S. Dai, S. Wu, Y. Dang, J. Chen, and G. Fang, "Novel detection method and parameters analysis of vital signal for ultra-wideband radar," in *2011 IEEE International Geoscience and Remote Sensing Symposium*, IEEE, 2011, pp. 1822–1825.

[37] Z. Li, W. Li, H. Lv, Y. Zhang, X. Jing, and J. Wang, "A novel method for respiration-like clutter cancellation in life detection by dual-frequency ir-uwb radar," *IEEE Transactions on Microwave Theory and Techniques*, vol. 61, no. 5, pp. 2086–2092, 2013.

[38] F. Khan and S. H. Cho, "A detailed algorithm for vital sign monitoring of a stationary/non-stationary human through ir-uwb radar," *Sensors*, vol. 17, no. 2, p. 290, 2017.

[39] A. Lazaro, D. Girbau, and R. Villarino, "Techniques for clutter suppression in the presence of body movements during the detection of respiratory activity through uwb radars," *Sensors*, vol. 14, no. 2, pp. 2595–2618, 2014.

[40] H. Shang, X. Zhang, Y. Ma, Z. Li, and C. Jin, "Random body movement cancellation method for fmcw radar vital sign detection," in *2019 IEEE International Conference on Signal, Information and Data Processing (ICSIDP)*, IEEE, 2019, pp. 1–4.

[41] L. Zhang, C. Ding, X. Zhou, H. Hong, C. Li, and X. Zhu, "Body movement cancellation using adaptive filtering technology for radar-based vital sign monitoring," in *2020 IEEE Radar Conference (RadarConf20)*, IEEE, 2020, pp. 1–5.

[42] M. Kagawa, N. Sasaki, K. Suzumura, and T. Matsui, "Sleep stage classification by body movement index and respiratory interval indices using multiple radar sensors," in *2015 37th Annual International Conference of the IEEE Engineering in Medicine and Biology Society (EMBC)*, IEEE, 2015, pp. 7606–7609.

[43] F. Zhu, K. Wang, and K. Wu, "Doppler radar techniques for vital signs detection featuring noise cancellation," in *2019 IEEE MTT-S International Microwave Biomedical Conference (IMBioC)*, IEEE, vol. 1, 2019, pp. 1–4.

[44] M.-C. Tang, C.-Y. Kuo, D.-C. Wun, F.-K. Wang, and T.-S. Horng, "A self-and mutually injection-locked radar system for monitoring vital signs in real time with random body movement cancellation," *IEEE Transactions on Microwave Theory and Techniques*, vol. 64, no. 12, pp. 4812–4822, 2016.

[45] C. Gu, G. Wang, Y. Li, T. Inoue, and C. Li, "A hybrid radar-camera sensing system with phase compensation for random body movement cancellation in doppler vital sign detection," *IEEE transactions on microwave theory and techniques*, vol. 61, no. 12, pp. 4678–4688, 2013.

[46] J.-M. Muñoz-Ferreras, J. Wang, Z. Peng, C. Li, and R. Gómez-García, "Fmcw-radar-based vital-sign monitoring of multiple patients," in *2019 IEEE MTT-S International Microwave Biomedical Conference (IMBioC)*, IEEE, vol. 1, 2019, pp. 1–3.

[47] M. Alizadeh, G. Shaker, J. C. M. De Almeida, P. P. Morita, and S. Safavi-Naeini, "Remote monitoring of human vital signs using mm-wave fmcw radar," *IEEE Access*, vol. 7, pp. 54 958–54 968, 2019.

[48] H. Lee, B.-H. Kim, J.-K. Park, and J.-G. Yook, "A novel vital-sign sensing algorithm for multiple subjects based on 24-ghz fmcw doppler radar," *Remote Sensing*, vol. 11, no. 10, p. 1237, 2019.

[49] H.-I. Choi, H. Song, and H.-C. Shin, "Target range selection of fmcw radar for accurate vital information extraction," *IEEE Access*, vol. 9, pp. 1261–1270, 2020.

[50] S. Ji, H. Wen, J. Wu, Z. Zhang, and K. Zhao, "Systematic heartbeat monitoring using a fmcw mm-wave radar," in *2021 IEEE International Conference on Consumer Electronics and Computer Engineering (ICCECE)*, IEEE, 2021, pp. 714–718.

[51] G. Welch, G. Bishop, *et al.*, "An introduction to the kalman filter," 1995.

[52] M. He, Y. Nian, and Y. Gong, "Novel signal processing method for vital sign monitoring using fmcw radar," *Biomedical Signal Processing and Control*, vol. 33, pp. 335–345, 2017.

[53] G. Beltrão, M. Alaee-Kerahroodi, U. Schroeder, D. Tatarinov, and B. S. MR, "Nonlinear least squares estimation for breathing monitoring using fmcw radars," in *2021 18th European Radar Conference (EuRAD)*, IEEE, 2022, pp. 241–244.

[54] X. Huang, L. Sun, T. Tian, Z. Huang, and E. Clancy, "Real-time non-contact infant respiratory monitoring using uwb radar," in *2015 IEEE 16th International Conference on Communication Technology (ICCT)*, IEEE, 2015, pp. 493–496.

[55] X. Hu and T. Jin, "Short-range vital signs sensing based on eemd and cwt using ir-uwb radar," *Sensors*, vol. 16, no. 12, p. 2025, 2016.

[56] R. Khaemphukhiao and P. Phasukkit, "Segmentation of 24ghz rf respiration signal using gmm," in *2019 12th Biomedical Engineering International Conference (BMEiCON)*, IEEE, 2019, pp. 1–5.

[57] A. Tekleab and M. Sanduleanu, "Vital signs detection using fmcw radar," in *2022 International Conference on Electrical and Computing Technologies and Applications (ICECTA)*, IEEE, 2022, pp. 51–54.

[58] Q. Lele, L. Shujie, G. Wenwen, M. Shuang, and Y. Tianhong, "Vital sign detection using multichannel fmcw radar," in *2021 CIE International Conference on Radar (Radar)*, IEEE, 2021, pp. 3027–3030.

[59] S. Wang, A. Pohl, T. Jaeschke, *et al.*, "A novel ultra-wideband 80 ghz fmcw radar system for contactless monitoring of vital signs," in *2015 37th Annual International Conference of the IEEE Engineering in Medicine and Biology Society (EMBC)*, IEEE, 2015, pp. 4978–4981.

[60] M. Giordano, G. Islamoglu, V. Potocnik, C. Vogt, and M. Magno, "Survey, analysis and comparison of radar technologies for embedded vital sign monitoring," in *2022 44th Annual International Conference of the IEEE Engineering in Medicine & Biology Society (EMBC)*, IEEE, 2022, pp. 854–860.

[61] W. Hu, H. Zhang, Z. Zhao, Y. Wang, and X. Wang, "Real-time remote vital sign detection using a portable doppler sensor system," in *2014 IEEE Sensors Applications Symposium (SAS)*, IEEE, 2014, pp. 89–93.

[62] Y. Xiong, S. Chen, X. Dong, Z. Peng, and W. Zhang, "Accurate measurement in doppler radar vital sign detection based on parameterized demodulation," *IEEE Transactions on Microwave Theory and Techniques*, vol. 65, no. 11, pp. 4483–4492, 2017.

[63] J. Le Kernec, F. Fioranelli, C. Ding, *et al.*, "Radar signal processing for sensing in assisted living: The challenges associated with real-time implementation of emerging algorithms," *IEEE Signal Processing Magazine*, vol. 36, no. 4, pp. 29–41, 2019.

[64] L. Sun, H. Hong, Y. Li, *et al.*, "Noncontact vital sign detection based on stepwise atomic norm minimization," *IEEE Signal Processing Letters*, vol. 22, no. 12, pp. 2479–2483, 2015.

[65] X. Huang, Z. Ju, and R. Zhang, "Real-time heart rate detection method based on 77 ghz fmcw radar," *Micromachines*, vol. 13, no. 11, p. 1960, 2022.

[66] R. Klein, *Bland-altman and correlation plot*, Last accessed 22 May 2023, 2023. [Online]. Available: https://www.mathworks.com/matlabcentral/fileexchange/45049-bland-altman-and-correlation-plot.

[67] J. M. Bland and D. G. Altman, "Measuring agreement in method comparison studies," *Statistical methods in medical research*, vol. 8, no. 2, pp. 135–160, 1999.

[68] G. Su, N. Petrov, and A. Yarovoy, "Dynamic estimation of vital signs with mmwave fmcw radar," in *2020 17th European Radar Conference (EuRAD)*, IEEE, 2021, pp. 206–209.

[69] G. Su, "Sequential estimator for breathing and heart beat frequencies using radar," 2019.

[70] V. Dham, "Programming chirp parameters in ti radar devices," 2020.

[71] Vernier, *Go direct respiration belt*, Last accessed 28 June 2023, 2023. [Online]. Available: https://www.vernier.com/product/go-direct-respiration-belt/.

[72] Viatom, *Checkme o2 max*, Last accessed 15 July 2023, 2022. [Online]. Available: https://www.viatomtech.com/checkmeo2-max.

[73] D. den Hoedt, "Dynamic vital sign estimation for multiple persons using mmwave technology," 2022.